Wiley
International Journal of Intelligent Systems
Volume 2024, Article ID 5510259, 23 pages
https://doi.org/10.1155/2024/5510259

WILEY

Research Article

Vibration Suppression and Trajectory Tracking Control of Flexible Joint Manipulator Based on PSO Algorithm and Fixed-Time Control

Yan Guan, Yang Wang, Rui Yin, Mingshu Chen, and Yaqi Xu

School of Computer Science, Xijing University, Xi'an 710123, China

Correspondence should be addressed to Yang Wang; zjt219571@163.com

Received 3 July 2023; Revised 6 May 2024; Accepted 9 May 2024; Published 1 June 2024

Academic Editor: Alexander Hošovský

In this paper, the vibration suppression and trajectory tracking control of a flexible joint manipulator (FJM) based on particle swarm optimization (PSO) and fixed-time nonsingular terminal sliding mode control (NTSMC) are studied. Firstly, in order to suppress the residual vibration of the FJM, an optimal trajectory planning method based on higher-order trajectory planning (HOTP) and the PSO algorithm is proposed. Then, to ensure that the FJM can track the optimized trajectory without being affected by the initial value of the trajectory, a novel fixed-time NTSMC scheme is proposed. Compared with the cubic spline trajectory, the proposed HOTP is smoother and can more accurately suppress the residual vibration of the FJM. By combining the HOTP with the PSO algorithm, the vibration amplitude of FJM can be suppressed to around 0.002 mm. Unlike finite-time NTSMC, the rate of convergence of the proposed fixed-time NTSMC does not depend on the initial value of FJM's joint trajectory. Especially when the initial value of the trajectory is large, the FJM can still quickly track the optimal trajectory within 0 to 1 s. Finally, the effectiveness of this method is verified through simulation and comparison.

1. Introduction

Flexible manipulators are widely used in aerospace, intelligent medical devices, and other fields because of their light weight, low energy consumption, and high flexibility [1–3]. In the work of the space station, the light, heavy, and high-precision the FJM can assist astronauts in completing some space missions. For example, satellite launch and recovery, space station assembly, and maintenance [4, 5]. However, due to the influence of flexible joints, the FJM has some residual vibration in the working process of the FJM, which seriously affects the positioning accuracy and working efficiency of the FJM [6, 7]. Therefore, studying FJM's vibration suppression and stability control is very important.

At present, numerous researchers have designed various trajectory plans for the FJM to eliminate residual vibration. Under the condition of continuous speed and acceleration of FJM's joints, different trajectories were designed, and the parameters involved in the trajectories were optimized to achieve the purpose of vibration reduction [8, 9]. Common joint trajectory planning includes cubic spline trajectory [10–12], the S-type trajectory [13–16], the composite trajectory, and other trajectories [17–20]. In [10], a cubic spline function was used to plan the FJM's joint, and then the PSO algorithm was used to find the optimal trajectory with the least amount of vibration. In [13], when the car moves according to the S-shaped trajectory, in order to suppress the unexpected load swing generated, a mechanism to prevent swing has been added to the S-shaped trajectory. Through an iterative learning strategy, the trajectory was continuously adjusted to ensure accurate positioning of the car. In [14], a bidirectional motion trajectory was designed for a flexible system with two degrees of freedom. A genetic algorithm was used to connect the forward trajectory with the reverse trajectory under the condition of satisfying the trajectory, thereby suppressing residual vibration in the system. In [17], An online trajectory correction scheme was designed for rigid, flexible robotic arms to plan the trajectory of the arm.

By adjusting the trajectory parameters to obtain the constraint conditions of the trajectory, the vibration suppression effect was achieved. In addition, for more complex flexible systems, due to the inherent characteristics of the system, it will generate certain vibrations. It is best to design trajectories with relatively few parameters on the basis of meeting the conditions, which are easy to apply in engineering. High-order interpolation trajectories can not only meet the constraint conditions of trajectories but also obtain accurate vibration optimization objective functions during the derivation process of vibration targets, which can more accurately suppress small vibrations and provide convenience for trajectory optimization.

In recent years, intelligent algorithms have been widely used in trajectory planning in various fields, especially in the field of flexible manipulators. Genetic algorithms [21], immune algorithms [22], neural network algorithms [23], chaotic algorithms [24], and ant colony algorithms [25] are considered the most common intelligent algorithms, all of which have their own characteristics and advantages and play an important role in solving different types of problems. In addition, deep learning technology has shown great potential in the control and optimization of robotic arms. It not only enhances the efficiency of robotic arm control but also enables more advanced autonomous decision-making and operation in unknown environments. For example, in [26], researchers applied a deep reinforcement learning strategy to satellites with ultra-long wings, developing an effective active control scheme to address vibration issues caused by external disturbances and self-rotation. This ensures the normal operation and longevity of the satellites. In [27], by employing the Coronavirus-inspired Group Immune Optimization (CHIO) method, the vibration controller gains of a flexible robotic arm were successfully optimized. In [28], the decision tree algorithm was employed to implement a parameter-tuned open-loop vibration control method for a multi-link flexible robotic arm, achieving effective suppression of residual and transient vibrations in control applications. In [29], a fuzzy neural network algorithm for PSO algorithm training was designed to solve the path planning problems of intelligent driving vehicles. The algorithm had a fast convergence speed and simple calculations. In order to address the issue of meteorological obstacles encountered by unmanned aerial vehicles during flight, they proposed a weather perception path planning method based on an enhanced intelligent water droplet algorithm in [30]. This method can ensure the flight safety of unmanned aerial vehicles. In [31], a new strategy combining neural network algorithms with discrete centralized planning was proposed for the complete coverage trajectory planning of autonomous underwater vehicles. In addition, the vibration frequencies of the robotic arm can be studied through various modeling techniques. In [32], the exploration of vibration frequencies in three different material robotic arms was conducted. The modeling techniques that align with the vibration frequencies are identified through the analysis of experimental data. Intelligent algorithms and deep learning technology have significantly enhanced the performance of robotic arms in control, vibration suppression, and path planning. These technologies enable the robotic arms to make precise and efficient autonomous decisions in unknown environments and fine-tune control strategies through simulation training, effectively reducing vibrations and enhancing adaptability.

On the basis of the optimal trajectory, in order to enable FJM's joints to quickly track the planned optimal trajectory, many scholars have used different control methods to solve this problem [33–35]. At present, the tracking control methods mainly include PID control [36–38], adaptive control [39, 40], and SMC [41–50]. SMC exhibits robustness and can effectively manage system uncertainty and external disturbances. However, in practical applications, the presence of nonlinear terms or parameter uncertainties in the control law leads to inherent jitter problems. Factors such as rapid switching of control modes, high-frequency oscillations, and sensitivity to control parameter errors contribute to this jitter [51]. Therefore, in practical applications, it is necessary to comprehensively consider these factors and adopt enhanced sliding mode control methods to mitigate or eliminate the impact of jitter, such as surpassing sliding mode control or continuous sliding mode control, in order to reduce system chatter. In [52], a model-based chatter-free sliding mode control algorithm was proposed to address the energy conversion issues in underground coal gasification processes. In [53], a robust nonlinear hybrid control method was employed to enhance the robustness of the multi-input multi-output, separately excited DC motor speed control system, thereby effectively addressing the chattering problem.

Especially in the field of robotics, SMC has received widespread attention for its ability to accurately control the position and posture of robots. In [35], this paper proposes a fractional-order SMC scheme for trajectory tracking control of Delta parallel robots. In [39], a novel adaptive barrier function integral terminal sliding mode controller has been designed for a quadcopter drone to solve its trajectory tracking problem. In [50], a continuous terminal SMC algorithm is proposed to enhance the robustness of servo motor systems. For the FJR system, due to factors such as strong coupling and uncertainty, as well as the presence of flexible components, certain vibrations may occur, making it difficult to achieve precise control. SMC is usually used for tracking control to enhance the robustness of the system. In [54], a terminal SMC was designed to ensure the convergence of the system in finite time. In [55, 56], for high-order uncertain systems, the use of observer and SMC joint control provides system robustness. However, when the initial value of the trajectory is large, the methods [54, 55] have a slow convergence speed and asymptotic stability, which may lead to slow trajectory tracking and affect the residual vibration of the FJM further. Recently, fixed-time SMC has been used for the tracking control of the FJM [40, 50]. Rsetam et al. have proficiently applied fixed-time SMC to FJM systems and achieved good control results [54–56]. Fixed-time SMC has a bounded convergence time and is independent of the initial state. Therefore, this paper designs a fixed-time

NTSMC that is not only independent of the initial trajectory value but also has faster tracking speed and smaller residual vibration for the FJM.

In conclusion, this paper proposes a vibration suppression control scheme that combines the HOTP and PSO algorithm. Firstly, based on the constraints of trajectory planning, HOTP trajectory was designed. Then, a mathematical model for residual vibration of the proposed trajectory planning function is theoretically derived, and the optimization objective function is obtained. Secondly, the PSO algorithm optimization objective function is used to achieve the effect of vibration suppression. Finally, in order to achieve FJM's joint tracking of the optimal trajectory, this paper designs a fixed-time NTSMC to control the trajectory. This method has the following advantages:

(1) Compared with the cubic spline trajectory in [10], this paper designs a HOTP that can not only meet the boundary conditions of joint angle, velocity, and acceleration but also make the trajectory smoother.

(2) The combination of the HOTP trajectory and the PSO algorithm solves the complex optimization problem in the trajectory planning of the FJM and effectively suppresses the vibration of the FJM.

(3) Unlike the asymptotic stability control schemes presented in [41, 42], the proposed NTSMC ensures fixed-time convergence of the tracking error, rather than fixed-time convergence to the sliding mode surface. In addition, fixed-time NTSMC can achieve higher convergence time precision and smaller initial control peaks.

The remaining content of this paper is arranged as follows: In Section 2, the necessary preliminary preparations for studying FJM are introduced, laying the foundation for vibration suppression and tracking control in the following text. This section mainly introduces the required assumptions, lemmas, the FJM model, and the research objectives of this article. Section 3 is the main body of this paper, which introduces the vibration suppression trajectory planning and tracking control based on the PSO algorithm to minimize the residual vibration of FJM. Firstly, we use HOTP trajectory to plan FJM and theoretically derive vibration optimization objectives. Then, optimize using the PSO algorithm. Finally, a controller was designed to track the optimal trajectory of FJM's joints, thereby increasing the stability of FJM. Section 4 is the simulation results section, which verifies the feasibility of the proposed method. Section 5 provides a summary of this article and describes the limitations of the research method.

2. Problem Description

This article has the following assumptions:

Assumption 1. For FJM system, the elastic effect is equivalent to that of a linear spring, with the elastic coefficient value of the linear spring serving as the joint's stiffness value. By understanding the joint stiffness values, it is possible to design practical vibration suppression measures to reduce vibrations caused by elasticity. This assumption is crucial for minimizing vibration interference in high-precision and high-performance applications.

Assumption 2. Do not consider the interference of other factors on the motor during rotation, and consider the motor rotor as a whole. This makes control strategies easier to comprehend and implement, reduces complexity in the control system, and enhances real-time control performance.

Assumption 3. T_e and T_s are the fixed-time parameters and $T_s > T_e > 0$. The choice of T_e and T_s directly influences the stability of the system. Ensuring that T_e is greater than T_s, and T_s is greater than zero which contributes to maintaining the stability of the system and preventing the occurrence of unstable behavior, especially in precision-critical applications with stringent control requirements.

The research object of this paper is the FJM. The system is mainly composed of the motor device, the deceleration device, the flexible joint device, and the load of FJM's arm. The system model of the FJM is shown in Figure 1. The meanings of the parameters in the FJM dynamic model are illustrated in Table 1.

This paper assumes that the joints of the FJM are linear springs. Then, dynamic modeling of the FJM is carried out using the Lagrange equation, and the following dynamic equation can be established [42].

$$\begin{cases} J_l\ddot{\eta} + K(\eta - \vartheta) = -Mgl\sin\eta, \\ J_m\ddot{\vartheta} + K(\vartheta - \eta) = \tau_m. \end{cases} \tag{1}$$

To facilitate the design of trajectory planning functions and tracking controllers, we define $x_1 = \eta$, $x_2 = \dot{\eta}$, $x_3 = \vartheta$, $x_4 = \dot{\vartheta}$, therefore, equation (1) is written as the following state equation:

$$\begin{cases} \dot{x}_1 = x_2, \\ \dot{x}_2 = \dfrac{K}{J_l}(x_3 - x_1) - \dfrac{Mgl}{J_l}\sin x_1, \\ \dot{x}_3 = x_4, \\ \dot{x}_4 = \dfrac{\tau_m}{J_m} + \dfrac{d}{J_m} - \dfrac{K}{J_m}(x_3 - x_1). \end{cases} \tag{2}$$

Assuming that the desired trajectory of the motor planning of the FJM is $\tilde{\vartheta}$, the trajectory error of the motor can be expressed as

$$e_1 = \tilde{\vartheta} - \vartheta. \tag{3}$$

The residual vibration error of the motor and joint of the FJM can be expressed as

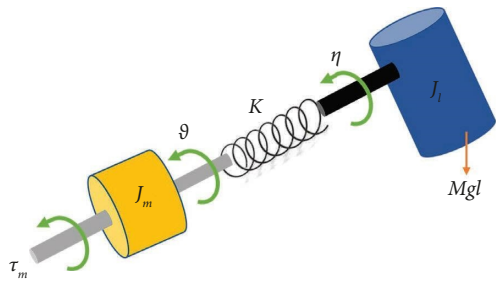

Figure 1: System model of the FJM.

$$E = \eta - \vartheta. \tag{4}$$

Then, we define $\dot{e}_1 = e_2$, $u = -(\tau_m/J_m)$, $\varphi = (K/J_m)(\tilde{\vartheta} - e_1 - x_1) + \ddot{\tilde{\vartheta}}$, the motor trajectory error equation of the FJM can be defined as

$$\begin{cases} \dot{e}_1 = e_2, \\ \dot{e}_2 = \ddot{\tilde{\vartheta}} - \dot{x}_4 = u + \varphi. \end{cases} \tag{5}$$

2.1. Fixed-Time Stability. Considering the following error state equations:

$$\begin{cases} \dot{e}_1 = e_2, \\ \dot{e}_2 = f(x) + u, \end{cases} \tag{6}$$

where e_1 and e_2 are the control errors of the system, $f(x)$ represents a nonlinear function, u is the control input of the system.

Definition 4. Finite-time stability

For system (6), if there is a finite time $T_f(e_1(0), e_2(0))$ that causes $\forall t \geq T_f(e_{1i}(0), e_{2i}(0))$: $e_{1i} = e_{2i} = 0$, then system (6) is finite-time stable.

Definition 5. Fixed-time stability

For system (6), if there is a finite time $T_f(e_1(0), e_2(0))$ that causes $\forall t \geq T_f(e_{1i}(0), e_{2i}(0))$: $e_{1i} = e_{2i} = 0$, and if there is a fixed constant $T_{\max}$ that causes $|T_f(e_{1i}(0), e_{2i}(0))| \leq T_{\max}$, then system (6) is fixed-time stable.

Lemma 6 (see [38]). *Considering the following dynamic system:*

$$\dot{L} = n, \tag{7}$$

where $L \in R$ denotes the system state and n denotes the control input and is designed as

$$n = n_1 = -\frac{\pi}{2T_s\mu}\left(\mathrm{Sig}(L)^{1-\mu} + \mathrm{Sig}(L)^{1+\mu}\right), \tag{8}$$

where $Sig(\cdot)$ is a sigmoid function and $Sig(\cdot) = (1/(1 + \exp(\cdot)))$. T_s is the fixed-time parameter and $0 < \mu < 1$, then $L = 0$ is fixed-time stable with the fixed-time T_s, and x converges to zero at time t_f

$$L(t) = 0, \quad \text{if } t \geq t_f, \tag{9}$$

$$\begin{aligned} t_f &= \frac{2T_s}{\pi}\arctan\left(\left|x(0)^{\alpha}\right|\right), \\ t_f &\leq T_s. \end{aligned} \tag{10}$$

Proof. Defining a Lyapunov function as

$$V = L^2. \tag{11}$$

Taking the derivative of t on both sides of equation (11) yields.

$$\dot{V} = 2L\dot{L}. \tag{12}$$

Combining equations (8) and (12), we can know

$$\begin{aligned} \frac{\mathrm{d}V}{\mathrm{d}t} &\leq -\frac{\pi}{T_s\mu}\left(|L|^{2-\mu} + |L|^{2+\mu}\right) \\ &= -\frac{\pi}{T_s\mu}\left(V^{((2-\mu)/2)} + V^{((2+\mu)/2)}\right). \end{aligned} \tag{13}$$

Furthermore, based on equation (13), we can conclude

$$\mathrm{d}t \leq \frac{T_f\mu}{\pi}\frac{-1}{V^{((2-\mu)/2)} + V^{((2+\mu)/2)}}\mathrm{d}V. \tag{14}$$

By integrating both sides of equation (14), the lower limit of the integration is $t = 0$, and the upper limit is $t = t_f$, we can know

$$\begin{aligned} t_f &\leq \int_{V(0)}^{V(t_f)} \frac{T_s\mu}{\pi}\frac{-1}{V^{((2-\mu)/2)} + V^{((2+\mu)/2)}}\mathrm{d}V \\ &= -\frac{T_s\mu}{\pi}\int_{V(0)}^{V(t_f)} \frac{V^{((2-\mu)/2)}}{1 + V^{(\mu/2)}}\mathrm{d}V \\ &= -\frac{T_s}{(\pi/2)}\int_{V(0)}^{V(t_f)} \frac{1}{1 + V^{\mu}}\mathrm{d}V^{(\mu/2)} \\ &= \frac{T_s}{(\pi/2)}\arctan\left(V^{(\mu/2)}(0)\right) - \frac{T_s}{(\pi/2)}\arctan\left(V^{(\mu/2)}(t_f)\right). \end{aligned} \tag{15}$$

Considering that $t = t_f$ is the upper bound for convergence time and $V(t_f) = 0$, if $L(0)$ is bounded, then equation (16) holds.

$$t_f \leq \frac{T_f}{(\pi/2)}\arctan\left(V^{\alpha}(0)\right) \leq T_s. \tag{16}$$

□

2.2. Motivation and Objective of This Paper

2.2.1. Motivation. We know that the FJM can generate residual vibration during movement. Currently, vibration can be suppressed through trajectory planning, but due to the interaction and complexity of the parameters in the trajectory, intelligent algorithms are needed to optimize the parameters in the trajectory. This paper designs a vibration reduction method that combines HOTP and PSO algorithm,

Table 1: The meaning of parameters in the FJM dynamic model.

Parameters	The meaning of parameters
η	The joint rotation angles of the FJM
ϑ	The motor rotation angles of the FJM
M	The quality of FJM's end-load
g	The gravitational acceleration of the end-load
l	The distance from the joint of the FJM to the center of mass of the end-load
τ_m	The control input for the FJM
K	The elastic stiffness of the FJM
J_l	The inertia of the joint end
J_m	The inertia of the motor rotor

which not only solves the problem of complex parameters in trajectory planning but also achieves the effect of vibration reduction. On this basis, in order to enable FJM's joint to track the optimized trajectory, the control schemes in [30–35] are all affected by the initial value of the trajectory. When the initial value of the trajectory is large, the convergence speed of trajectory tracking will significantly slow down. This paper will design a fixed-time NTSMC that is not affected by the initial trajectory and has a faster trajectory tracking speed.

2.2.2. Objective. This paper aims to plan an optimal and minimum vibration trajectory for FJM using a combination of HOTP and PSO algorithm methods to plan and suppress vibration, i.e., $E = \eta - \vartheta = 0$. Then, a fixed-time NTSMC was designed to track the optimization trajectory, ultimately causing the control objective $e_1 = \widetilde{\vartheta} - \vartheta$ to approach zero.

3. Main Result

3.1. Derivation of Residual Vibration Based on the HOTP. When planning the joints of the FJM, we first need to clarify the starting and target points of the trajectory. Then, different interpolation methods are used to plan the joints. Finally, a complete joint trajectory can be obtained. In this section, a variable parameter HOTP function is proposed to plan the trajectory of the FJM, and the residual vibration optimization objective function of the FJM is obtained through theoretical calculation.

Let $\omega = \sqrt{K/J_l}$, $\widetilde{\vartheta} = \vartheta - (Mgl/K)\sin\eta$, the joint model in the dynamic equation of FJM (1) can be transformed into

$$\ddot{\eta} = \omega^2(\widetilde{\vartheta} - \eta). \tag{17}$$

The design variable parameter HOTP motor track is

$$\vartheta = \left(\eta_f - \eta_0\right)\sum_{i=0}^{6}\varepsilon_i(\varpi)^i + \eta_0 + \frac{Mgl}{K}\sin\eta, \tag{18}$$

where $\varpi = (t/t_f)$, t_f is planning time, $\varepsilon_i (i = 0, 2, \ldots, 6)$ is unknown parameter.

Combining equation (18) and $\widetilde{\vartheta} = \vartheta - (Mgl/K)\sin\eta$, the motor expected trajectory can be designed as

$$\widetilde{\vartheta} = \left(\eta_f - \eta_0\right)\sum_{i=0}^{6}\varepsilon_i(\varpi)^i + \eta_0. \tag{19}$$

The angular velocity and angular acceleration of the trajectory planning motor can be determined by calculating the derivative of (19):

$$\dot{\widetilde{\vartheta}} = \frac{\left(\eta_f - \eta_0\right)}{t_f}\left[6\varepsilon_6(\varpi)^5 + 5\varepsilon_5(\varpi)^4 + 4\varepsilon_4(\varpi)^3 + 3\varepsilon_3(\varpi)^2 + 2\varepsilon_2\varpi + \frac{\varepsilon_1}{t_f}\right], \tag{20}$$

$$\ddot{\widetilde{\vartheta}} = \frac{\left(\eta_f - \eta_0\right)}{t_f^2}\left[30\varepsilon_6(\varpi)^4 + 20\varepsilon_5(\varpi)^3 + 12\varepsilon_4(\varpi)^2 + 6\varepsilon_3\varpi + \frac{2\varepsilon_2}{t_f}\right], \tag{21}$$

The joint trajectory of FJM must be smooth, continuous, and meet the initial time $(t = 0)$ and target time $(t = t_f)$ constraints in terms of trajectory, velocity, and acceleration as follows:

$$\begin{cases} \eta(t=0) = \eta_0, \eta\left(t = t_f\right) = \eta_f, \\ \dot{\eta}(t=0) = 0, \dot{\eta}\left(t = t_f\right) = 0, \\ \ddot{\eta}(t=0) = 0, \ddot{\eta}\left(t = t_f\right) = 0. \end{cases} \tag{22}$$

Combining equations (19)–(22), we can obtain the values and relationship expressions of certain parameters of the variable parameter HOTP as

$$\begin{cases} \varepsilon_0 = \varepsilon_1 = \varepsilon_2 = 0, \\ \varepsilon_6 + \varepsilon_5 + \varepsilon_4 + \varepsilon_3 + \varepsilon_2 + \varepsilon_1 = 1, \\ 6\varepsilon_6 + 5\varepsilon_5 + 4\varepsilon_4 + 3\varepsilon_3 + 2\varepsilon_2 + \dfrac{\varepsilon_1}{t_f} = 0, \\ 30\varepsilon_6 + 20\varepsilon_5 + 12\varepsilon_4 + 6\varepsilon_3 + \dfrac{2\varepsilon_2}{t_f} = 0. \end{cases} \tag{23}$$

The relationship between ε_0, ε_1, t_f and ε_3, ε_4, ε_5 can be determined by solving equation (23):

$$\begin{cases} \varepsilon_0 = \varepsilon_2 = 0, \\ \varepsilon_3 = 10 - 10\varepsilon_0 - 10\varepsilon_1, \\ \varepsilon_4 = -15 + 15\varepsilon_0 + 15\varepsilon_1 + \dfrac{\varepsilon_1}{t_f}, \\ \varepsilon_5 = 6 - 6\varepsilon_0 - 6\varepsilon_1 - \dfrac{\varepsilon_1}{t_f}. \end{cases} \tag{24}$$

The mathematical model of residual vibration can be easily solved by normalizing the variable parameter HOTP, as illustrated in equation (25):

$$\overline{\vartheta} = \begin{cases} \varepsilon_6(\varpi)^6 + \varepsilon_5(\varpi)^5 + \varepsilon_4(\varpi)^4 + \varepsilon_3(\varpi)^3 + \varepsilon_2(\varpi)^2 + \varepsilon_1\varpi + \varepsilon_0, & t \le t_f, \\ 1, & t > t_f. \end{cases} \tag{25}$$

The vibration analysis of FJM during and after movement is as follows.

3.1.1. During Movement $0 \le t \le t_f$. The joint trajectory and tracking error of FJM during motion can be determined by substituting equation (25) into dynamic (17)

$$\ddot{\eta} + \omega^2\eta = \omega^2\left(\varepsilon_6(\varpi)^6 + \varepsilon_5(\varpi)^5 + \varepsilon_4(\varpi)^4 + \varepsilon_3(\varpi)^3 + \varepsilon_2(\varpi)^2 + \varepsilon_1\varpi + \varepsilon_0\right). \tag{26}$$

Equation (26) is simplified to

$$\ddot{\eta} + \omega^2\eta = \omega^2\varepsilon_6(\varpi)^6 + \omega^2\varepsilon_5(\varpi)^5 + \omega^2\varepsilon_4(\varpi)^4 + \omega^2\varepsilon_3(\varpi)^3 + \omega^2\varepsilon_2(\varpi)^2 + \omega^2\varepsilon_1\varpi + \omega^2\varepsilon_0. \tag{27}$$

Equation (27) is a second-order nonhomogeneous differential equation. First, we need to solve the general solution of the homogeneous equation of (27), and the corresponding homogeneous equation is

$$\ddot{\eta} + \omega^2\eta = 0. \tag{28}$$

The characteristic equation corresponding to equation (28) is

$$\lambda^2 + \omega^2 = 0. \tag{29}$$

According to equation (29), the characteristic root of equation (28) can be solved as

$$\begin{cases} \lambda_1 = \omega i, \\ \lambda_2 = -\omega i. \end{cases} \tag{30}$$

The characteristic root is a pair of imaginary roots, so the general solution of the homogeneous equation can be written as

$$\eta^o = C_1\cos(\omega t) + C_2\sin(\omega t). \tag{31}$$

Then solve a special solution of equation (27), and let its special solution be η^*

$$\eta^* = A_6t^6 + A_5t^5 + A_4t^4 + A_3t^3 + A_2t^2 + A_1t + A_0. \tag{32}$$

Calculating the first derivative and the second derivative of equation (32) as follows:

$$\begin{aligned} \dot{\eta}^* &= 6A_6t^5 + 5A_5t^4 + 4A_4t^3 + 3A_3t^2 + 2A_2t + A_1, \\ \ddot{\eta}^* &= 30A_6t^4 + 20A_5t^3 + 12A_4t^2 + 6A_3t + 2A_2. \end{aligned} \tag{33}$$

Substituting equations (32) and (33) into (27):

$$\begin{aligned} &30A_6t^4 + 20A_5t^3 + 12A_4t^2 + 6A_3t + 2A_2 + \omega^2 \\ &\left(A_6t^6 + A_5t^5 + A_4t^4 + A_3t^3 + A_2t^2 + A_1t + A_0\right) \\ &= \omega^2\varepsilon_6(\varpi)^6 + \omega^2\varepsilon_5(\varpi)^5 + \omega^2\varepsilon_4(\varpi)^4 + \omega^2\varepsilon_3(\varpi)^3 + \omega^2\varepsilon_2(\varpi)^2 + \omega^2\varepsilon_1\varpi + \omega^2\varepsilon_0. \end{aligned} \tag{34}$$

According to the undetermined coefficient method, the relationship equation of corresponding parameters can be obtained as

$$\begin{cases} \omega^2 A_6 = \dfrac{\omega^2\varepsilon_6}{t_f^6}, \\ \omega^2 A_5 = \dfrac{\omega^2\varepsilon_5}{t_f^5}, \\ \omega^2 A_4 = \dfrac{\omega^2\varepsilon_4}{t_f^4}, \\ 20A_5 + \omega^2 A_3 = \dfrac{\omega^2\varepsilon_3}{t_f^3}, \\ 12A_4 + \omega^2 A_2 = \dfrac{\omega^2\varepsilon_2}{t_f^2}, \\ 6A_3 + \omega^2 A_1 = \dfrac{\omega^2\varepsilon_1}{t_f}, \\ 2A_2 + \omega^2 A_0 = \omega^2\varepsilon_0. \end{cases} \tag{35}$$

According to (35), we can find that the coefficient of the special solution is

$$\begin{cases} A_6 = \dfrac{\varepsilon_6}{t_f^6}, \\ A_5 = \dfrac{\varepsilon_5}{t_f^5}, \\ A_4 = \dfrac{\varepsilon_4}{t_f^4}, \\ A_3 = \dfrac{\varepsilon_3}{t_f^3} - \dfrac{20\varepsilon_5}{t_f^5\omega^2}, \\ A_2 = \dfrac{\varepsilon_2}{t_f^2} - \dfrac{12\varepsilon_4}{t_f^4\omega^2}, \\ A_1 = \dfrac{\varepsilon_1}{t_f} - \dfrac{6\varepsilon_3}{t_f^3\omega^2} + \dfrac{120\varepsilon_5}{t_f^5\omega^4}, \\ A_0 = \varepsilon_0 - \dfrac{2\varepsilon_2}{t_f^2\omega^2} + \dfrac{24\varepsilon_4}{t_f^4\omega^4}. \end{cases} \tag{36}$$

Therefore, special solution η^* is

$$\begin{aligned} \eta^* &= \varepsilon_6\varpi^6 + \varepsilon_5\varpi^5 + \varepsilon_4\varpi^4 + \left(\frac{\varepsilon_3}{t_f^3} - \frac{20\varepsilon_5}{t_f^5\omega^2}\right)t^3 + \left(\frac{\varepsilon_2}{t_f^2} - \frac{12\varepsilon_4}{t_f^4\omega^2}\right)t^2 \\ &+ \left(\frac{\varepsilon_1}{t_f} - \frac{6\varepsilon_3}{t_f^3\omega^2} + \frac{120\varepsilon_5}{t_f^5\omega^4}\right)t + \varepsilon_0 - \frac{2\varepsilon_2}{t_f^2\omega^2} + \frac{24\varepsilon_4}{t_f^4\omega^4}. \end{aligned} \tag{37}$$

The solution of equation (27) is equal to the homogeneous general solution plus the nonhomogeneous special solution as follows:

$$\eta = \eta^{o} + \eta^{*} = C_1 \cos(\omega t) + C_2 \sin(\omega t) \cdot \varepsilon_6 \varpi^6 + \varepsilon_5 \varpi^5 + \varepsilon_4 \varpi^4 + \left(\frac{\varepsilon_3}{t_f^3} - \frac{20\varepsilon_5}{t_f^5 \omega^2}\right) t^3 + \left(\frac{\varepsilon_2}{t_f^2} - \frac{12\varepsilon_4}{t_f^4 \omega^2}\right) t^2 + \left(\frac{\varepsilon_1}{t_f} - \frac{6\varepsilon_3}{t_f^3 \omega^2} + \frac{120\varepsilon_5}{t_f^5 \omega^4}\right) t + \varepsilon_0 - \frac{2\varepsilon_2}{t_f^2 \omega^2} + \frac{24\varepsilon_4}{t_f^4 \omega^4}. \tag{38}$$

Because the initial value of the system is $\dot{\eta}(0) = 0, \ddot{\eta}(0) = 0$, we determine C_1, C_2 is

$$C_2 = -\frac{\varepsilon_1}{t_f \omega} + \frac{6\varepsilon_3}{t_f^3 \omega^3} - \frac{120\varepsilon_5}{t_f^5 \omega^5}, \quad C_1 = 2\left(\frac{\varepsilon_2}{t_f^2 \omega^2} - \frac{12\varepsilon_4}{t_f^4 \omega^4}\right). \tag{39}$$

Combining (38) and (39), the joint trajectory of the FJM can be obtained as

$$\eta = \left(\frac{2\varepsilon_2}{t_f^2 \omega^2} - \frac{24\varepsilon_4}{t_f^4 \omega^4}\right) \cos(\omega t) + \left(-\frac{\varepsilon_1}{t_f \omega} + \frac{6\varepsilon_3}{t_f^3 \omega^3} - \frac{120\varepsilon_5}{t_f^5 \omega^5}\right) \sin(\omega t) + \varepsilon_6 \varpi^6 + \varepsilon_5 \varpi^5 + \varepsilon_4 \varpi^4 + \left(\frac{\varepsilon_3}{t_f^3} - \frac{20\varepsilon_5}{t_f^5 \omega^2}\right) t^3 + \left(\frac{\varepsilon_2}{t_f^2} - \frac{12\varepsilon_4}{t_f^4 \omega^2}\right) t^2 + \left(\frac{\varepsilon_1}{t_f} - \frac{6\varepsilon_3}{t_f^3 \omega^2} + \frac{120\varepsilon_5}{t_f^5 \omega^4}\right) t + \varepsilon_0 - \frac{2\varepsilon_2}{t_f^2 \omega^2} + \frac{24\varepsilon_4}{t_f^4 \omega^4}. \tag{40}$$

Therefore, the error of the FJM in the movement process is

$$\xi\eta = \left(\frac{2\varepsilon_2}{t_f^2 \omega^2} - \frac{24\varepsilon_4}{t_f^4 \omega^4}\right) \cos(\omega t) + \left(-\frac{\varepsilon_1}{t_f \omega} + \frac{6\varepsilon_3}{t_f^3 \omega^3} - \frac{120\varepsilon_5}{t_f^5 \omega^5}\right) \sin(\omega t) - \frac{20\varepsilon_5}{t_f^5 \omega^2} t^3 - \frac{12\varepsilon_4}{t_f^4 \omega^2} t^2 + \left(-\frac{6\varepsilon_3}{t_f^3 \omega^2} + \frac{120\varepsilon_5}{t_f^5 \omega^4}\right) t - \frac{2\varepsilon_2}{t_f^2 \omega^2} + \frac{24\varepsilon_4}{t_f^4 \omega^4}. \tag{41}$$

3.1.2. End of Movement $t > t_f$. The joint model of the FJM can be expressed after the movement as follows:

$$\ddot{\eta} = \omega^2 (1 - \eta). \tag{42}$$

The time of trajectory planning ranges from $t_f \longrightarrow t - t_f$.

The residual error after the FJM motion is determined by the initial values $\eta(t - t_f) = \eta_f, \dot{\eta}(t - t_f) = \dot{\eta}_f$ as

$$\begin{cases} \eta = \left(\eta_{t_f} - 1\right) \cos\left(\omega\left(t - t_f\right)\right) + \dfrac{\dot{\eta}_{t_f}}{\omega} \sin\left(\omega\left(t - t_f\right)\right) + 1, \\ \xi\eta = \left(\eta_{t_f} - 1\right) \cos\left(\omega\left(t - t_f\right)\right) + \dfrac{\dot{\eta}_{t_f}}{\omega} \sin\left(\omega\left(t - t_f\right)\right), \end{cases} \tag{43}$$

where $\eta_{tf} = \eta(t = t_f)$, $\dot{\eta}_{tf} = \dot{\eta}(t = t_f)$.

According to $\eta_{tf} = \eta(t = t_f)$, $\dot{\eta}_{tf} = \dot{\eta}(t = t_f)$, η_{tf}, and $\dot{\eta}_{tf}$ can be calculated by combining equation (43) as

$$\begin{cases} \eta_{tf} = \left(\dfrac{2\varepsilon_2}{t_f^2\omega^2} - \dfrac{24\varepsilon_4}{t_f^4\omega^4}\right)\cos\left(\omega t_f\right) + \left(-\dfrac{\varepsilon_1}{t_f\omega} + \dfrac{6\varepsilon_3}{t_f^3\omega^3} - \dfrac{120\varepsilon_5}{t_f^5\omega^5}\right)\sin\left(\omega t_f\right) \\ \quad + \varepsilon_5 + \varepsilon_4 + \varepsilon_3 + \varepsilon_2 + \varepsilon_1 + \varepsilon_0 - \dfrac{20\varepsilon_5}{t_f^2\omega^2} - \dfrac{12\varepsilon_4}{t_f^2\omega^2} - \dfrac{6\varepsilon_3}{t_f^2\omega^2} + \dfrac{120\varepsilon_5}{t_f^4\omega^4} - \dfrac{2\varepsilon_2}{t_f^2\omega^2} + \dfrac{24\varepsilon_4}{t_f^4\omega^4}, \\ \dot{\eta}_{tf} = -\left(\dfrac{2\varepsilon_2}{t_f^2\omega^2} - \dfrac{24\varepsilon_4}{t_f^4\omega^4}\right)\omega\sin(\omega t) + \left(-\dfrac{\varepsilon_1}{t_f\omega} + \dfrac{6\varepsilon_3}{t_f^3\omega^3} - \dfrac{120\varepsilon_5}{t_f^5\omega^5}\right)\omega\cos(\omega t) \\ \quad + \dfrac{5\varepsilon_5}{t_f^5}t^4 + \dfrac{4\varepsilon_4}{t_f^4}t^3 + \left(\dfrac{3\varepsilon_3}{t_f^3} - \dfrac{60\varepsilon_5}{t_f^5\omega^2}\right)t^2 + \left(\dfrac{2\varepsilon_2}{t_f^2} - \dfrac{24\varepsilon_4}{t_f^4\omega^2}\right)t + \dfrac{\varepsilon_1}{t_f} - \dfrac{6\varepsilon_3}{t_f^3\omega^2} + \dfrac{120\varepsilon_5}{t_f^5\omega^4}. \end{cases} \tag{44}$$

The residual vibration amplitude A can be calculated when combined with equations (44), resulting in the final optimization objective function as

$$A^2 = \left(\eta_{t_f} - 1\right)^2 + \left(\frac{\dot{\eta}_{t_f}}{\omega}\right)^2 = \frac{\left(\begin{array}{c} \varepsilon_0 + \varepsilon_1 + \varepsilon_2 + \varepsilon_3 + \varepsilon_4 + \varepsilon_5 + \cos\left(\omega t_f\right)\left(\left(2\varepsilon_2/\omega^2 t_f^2\right) - \left(24\varepsilon_4/\omega^4 t_f^4\right)\right) - \sin\left(\omega t_f\right) \\ \left(\left(\varepsilon_1/\omega t_f\right) - \left(6\varepsilon_3/\omega^3 t_f^3\right) + \left(120\varepsilon_5/\omega^5 t_f^5\right)\right) - \left(2\varepsilon_2/\omega^2 t_f^2\right) - \left(6\varepsilon_3/\omega^2 t_f^2\right) + \left(12\varepsilon_4/\omega^2 t_f^2\right) - \left(20\varepsilon_5/\omega^2 t_f^2\right) + \left(24\varepsilon_4/\omega^4 t_f^4\right) + \left(120\varepsilon_5/\omega^4 t_f^4\right) - 1 \end{array}\right)^2 + \left(\begin{array}{c} t_f\left(\left(2\varepsilon_2/t_f^2\right) - \left(24\varepsilon_4/\omega^2 t_f^4\right)\right) + t_f^2\left(\left(3\varepsilon_3/t_f^3\right) - \left(60\varepsilon_5/\omega^2 t_f^5\right)\right) + \left(\varepsilon_1/t_f\right) + \left(4\varepsilon_4/t_f\right) + \left(5\varepsilon_5/t_f\right) - \left(6\varepsilon_3/\omega^2 t_f^3\right) + \left(120\varepsilon_5/\omega^4 t_f^5\right) \\ -\omega\sin\left(\omega t_f\right)\left(\left(2\varepsilon_2/\omega^2 t_f^2\right) - \left(24\varepsilon_4/\omega^4 t_f^4\right)\right) - \omega\cos\left(\omega t_f\right)\left(\left(\varepsilon_1/\omega t_f\right) - \left(6\varepsilon_3/\omega^3 t_f^3\right) + \left(120\varepsilon_5/\omega^5 t_f^5\right)\right) \end{array}\right)^2}{\omega^2} \tag{45}$$

3.2. Optimization of Residual Vibration Based on HOTP and PSO Algorithms. In order to suppress the residual vibration of the FJM, this paper uses the PSO algorithm to optimize the parameters in the HOTP. First, the PSO algorithm can solve the parameter coefficient value of HOTP randomly. Then, the PSO algorithm searches for the optimal solution in the random solution through iteration and mainly evaluates the accuracy of the solution according to its fitness (the target value to be optimized), which has the advantages of easy implementation, high accuracy, and fast convergence.

Step 1. According to the constraint conditions (22), the relationship between HOTP parameters can be solved using equation (23), and (24) is converted into matrix equation form (46) to facilitate parameter observation.

$$\begin{pmatrix} 1 & 1 & 1 \\ 5 & 4 & 3 \\ 20 & 12 & 6 \end{pmatrix}\begin{pmatrix} \varepsilon_5 \\ \varepsilon_4 \\ \varepsilon_3 \end{pmatrix} = \begin{pmatrix} 1 - \varepsilon_6 \\ -6\varepsilon_6 \\ -30\varepsilon_6 \end{pmatrix}. \tag{46}$$

The relationship between a_6 and other parameters can be resolved by combining (46)

$$\begin{cases} \varepsilon_0 = \varepsilon_1 = \varepsilon_2 = 0, \\ \varepsilon_3 = 10 - \varepsilon_6, \\ \varepsilon_4 = -15 + 3\varepsilon_6, \\ \varepsilon_5 = 6 - 3\varepsilon_6. \end{cases} \tag{47}$$

Step 2. Research reveals the final residual vibration model is linked to planning time t_f and parameter a_6, forming a dual parameter objective optimization problem. The ultimate objective optimization function can be expressed as

$$A = f\left(\varepsilon_6, t_f\right). \tag{48}$$

The PSO algorithm and Simulink are utilized to optimize the trajectory parameters of FJM, aiming to minimize residual vibration, as illustrated in Figure 2.

3.3. Design of Fixed-Time Nonsingular Sliding Mode Tracking Control. On the basis of the optimal trajectory in the previous section, this section will design a fixed-time sliding mode controller to enable FJM's joint to quickly track the optimal trajectory. The fixed-time sliding surface of system (5) can be designed according to Lemma 6 as follows:

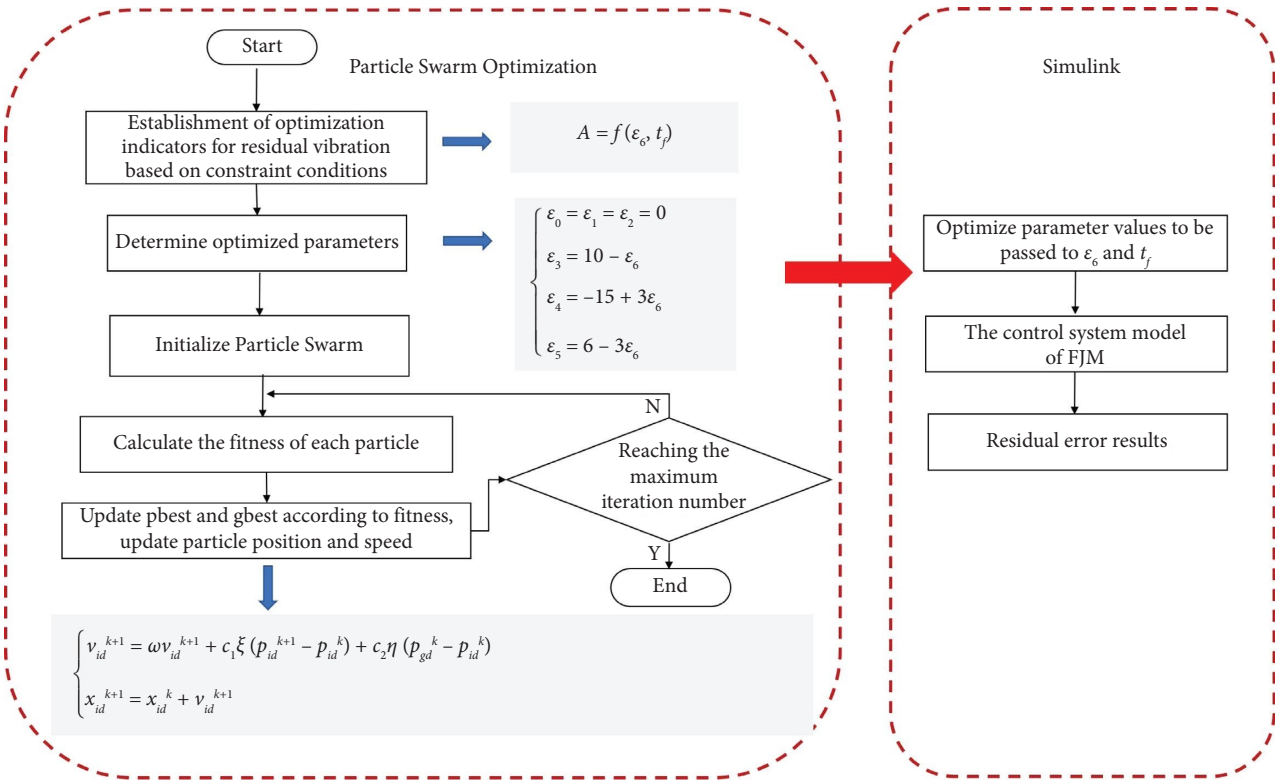

Figure 2: Flowchart of PSO algorithm.

$$s = e_2 - \frac{\pi}{2(T_e - T_s)\alpha}\left(f_{e1} + \operatorname{sig}(e_1)^{1+\alpha}\right), \tag{49}$$

where T_e and T_s are the fixed-time parameters and $T_s > T_e > 0$. α satisfies $0 < \alpha < 1$. The nonlinear function f_{e1} can be defined as follows:

$$f_{e_1} = \begin{cases} \dfrac{-1 - \ln\xi}{1 - \alpha - \xi\ln\xi}|e_1|^{2-\alpha}\operatorname{sign}(e_1) + \dfrac{\xi^{-2\alpha}\xi^{|e_1|}}{1 - \alpha - \xi\ln\xi}e_1, & |e_1| \le \xi \\ |e_1|^{1-\alpha}\operatorname{sig}(e_1), & |e_1| > \xi. \end{cases} \tag{50}$$

Equation (50) states that f_{e1} is differentiable, and its derivative is given as

$$\dot{f}_{e_1} = \begin{cases} \left(\dfrac{-1 - \ln\xi}{1 - \alpha - \xi\ln\xi}(2 - \alpha)|e_1|^{1-\alpha} + \dfrac{\xi^{-2\alpha}}{1 - \alpha - \xi\ln\xi}\left(|e_1|\ln\xi + 1\right)\xi^{|e1|}\right)e_2, & |e_1| \le \xi, \\ (1 - \alpha)|e_1|^{-\alpha}e_2, & |e_1| > \xi, \end{cases} \tag{51}$$

where $\xi \in (0, (1/e)) = (0, 0.36)$ and $\xi = \alpha$.

According to equation (51), if $e_1 = 0$, $\dot{f}_{e_1} = (\xi^{-2\alpha}/(1 - \alpha - \xi\ln\xi))e_2$. Therefore, it can be concluded that the function $\dot{f}_{e_1}$ is continuous in $e_1 = 0$ and has no non-singular points. The curves are shown in Figures 3 and 4.

The time derivative of (49) can be calculated as

$$\dot{s} = \dot{e}_2 - \frac{\pi}{2(T_e - T_s)\alpha}\left(\dot{f}_{e1} + (1 + \alpha)|e_1|^{\alpha}e_2\right). \tag{52}$$

From the error equation and (52), we have

$$\dot{s} = u + \varphi - \frac{\pi}{2(T_e - T_s)\alpha}\left(\dot{f}_{e1} + (1 + \alpha)|e_1|^{\alpha}e_2\right). \tag{53}$$

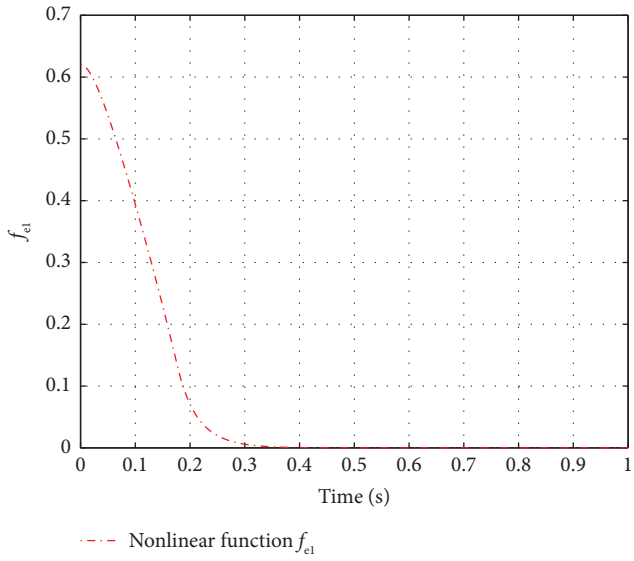

FIGURE 3: Nonlinear function f_{e_1}.

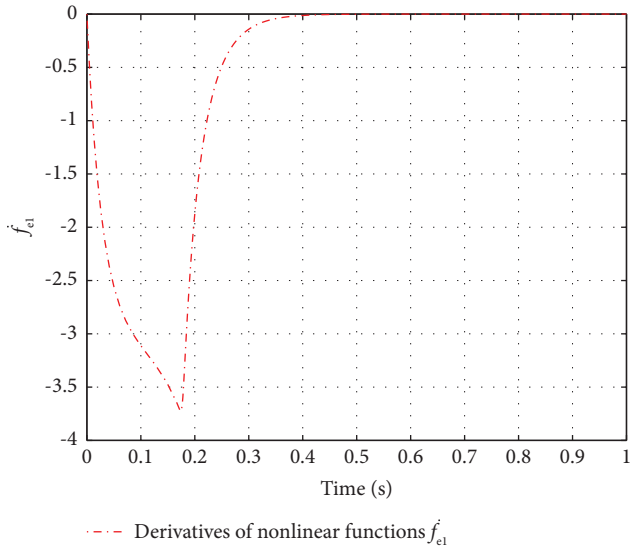

FIGURE 4: Derivatives of nonlinear function $\dot{f}_{e_1}$.

According to the sliding surface (49), the controller of fixed-time NTSMC can be designed as

$$u = -\varphi + \frac{\pi}{2(T_e - T_s)\alpha}\left(\dot{f}_{e1} + (1+\alpha)\,|e_1|^{\alpha} e_2\right) - \frac{\pi}{2T_s\alpha_s}\left(\mathrm{sig}(s)^{1+\alpha_s} + \mathrm{sig}(s)^{1-\alpha_s}\right). \tag{54}$$

Theorem 7. *For FJM system (5), control scheme (54) can guarantee that the tracking errors e_1 converge to the following small region in fixed time T_s.*

$$e_1 \le \xi, \quad \text{if } t \ge T_s, \tag{55}$$

then, e_1 can arrive at the origin asymptotically. The proof of Theorem 7 is provided in Appendix A.

4. Simulation Results

4.1. Residual Vibration Simulation Results of Trajectory Planning. In this section, the parameters of the FJM's model are chosen as $K = 120\,\mathrm{N{\cdot}m/rad}$, $J_m = 10\,\mathrm{kg{\cdot}m^2}$, $J_l = 8\mathrm{kg{\cdot}m^2}$, and $Mgl = 10\mathrm{N}$.

Case 1 (Change planning time): The initial angle of FJM's joint is $\eta_0 = 10^{\circ}$, the target angle is $\eta_f = 45^{\circ}$, and the change is t_f from 3 s to 5 s. HOTP's angle, velocity, and acceleration are shown in Figure 5(a)–5(c).

Case 2 (Change initial angle): the target angle $\eta_f = 45^{\circ}$, planning time $t_f = 3$, change the initial angle from 0° to 10°, at this time, HOTP's angle, velocity and acceleration are shown in Figure 6(a)–6(c).

Case 3 (Comparing cubic spline trajectories): The initial angle of FJM's joint is $\eta_0 = 0^{\circ}$, the target angle is $\eta_f = 10^{\circ}$, planning time is $t_f = 3$, The comparison of the angle, velocity, and acceleration between the cubic spline trajectory in reference [10] and the HOTP trajectory is shown in Figures 7(a)–7(c).

The ideal tracking trajectory of FJM's joint can be chosen as follows:

$$\begin{cases} \widetilde{\vartheta} = \left(\eta_f - \eta_0\right)\sum_{i=0}^{6} \varepsilon_i\,(\varpi)^i + \eta_0, \\ \varepsilon_0 = \varepsilon_1 = \varepsilon_2 = 0, \\ \varepsilon_3 = 9, \\ \varepsilon_4 = -12, \\ \varepsilon_5 = 3, \\ \varepsilon_6 = 1. \end{cases} \tag{56}$$

From Figures 5 and 6, it is evident that under various initial angles, target angles, and planned times, the HOTP trajectory exhibits exceptional smoothness and continuity. Further examination of Figure 7 reveals that the HOTP trajectory maintains continuity in acceleration, whereas the cubic spline trajectory shows discontinuities in acceleration. These discontinuities can cause sudden changes in the forces acting on a flexible robotic arm, leading to system vibrations. In high-speed motion control scenarios, these vibrations can negatively affect the overall performance of the system, severely compromising the stability and precision of the machinery.

After verifying the continuity of HTOP, the PSO algorithm is used to optimize HOTP to minimize the residual vibration of the FJM. The process of combining the PSO algorithm with Simulink is as follows:

(1) Optimize vibration target: the objective equation for optimizing residual vibration of flexible joints is presented in (45).

(2) Determine the parameter that needs to be optimized: a_6, t_f in the high-order interpolation trajectory of the flexible joint.

(3) Initialize particle swarm: select the maximum inertia weight $\omega_{\max} = 0.8$, with a minimum value of

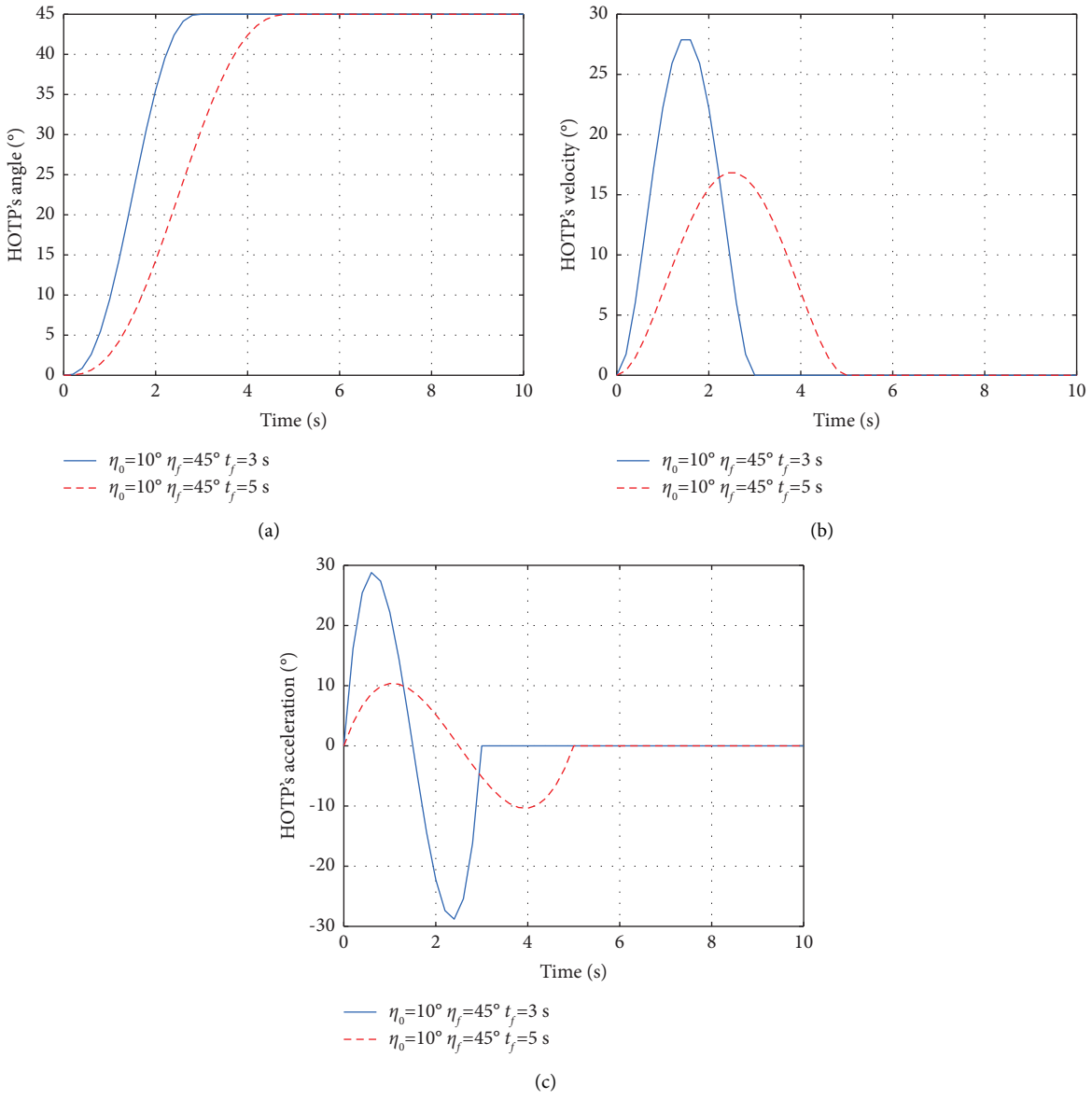

Figure 5: HOTP's trajectory for changing planning time based on Case 1. (a) HOTP's angle. (b) HOTP's velocity. (c) HOTP's acceleration.

$\omega_{\min} = 0.4$, acceleration constant $c_1 = c_2 = 2$, dimension $d = 2$, particle swarm size $N = 50$, and randomly generate initial particle swarm values and velocities.

(4) Calculate the fitness of each particle: combine equation (45) to calculate the corresponding vibration amplitude of the initial particle.

(5) Update particle position and velocity: the velocity represents the displacement of the particle in continuous iterations, and the fitness value determines the quality of the solution. During the continuous iteration of particles towards better features, individual extrema and global extrema are constantly updated. The update formula is as follows:

$$\begin{cases} v_{id}^{k+1} = \omega v_{id}^{k+1} + c_1 \xi\left(p_{id}^{k+1} - p_{id}^{k}\right) + c_2 \eta\left(p_{gd}^{k} - p_{id}^{k}\right), \\ x_{id}^{k+1} = x_{id}^{k} + v_{id}^{k+1}, \end{cases} \tag{57}$$

where x_{id} represents the position of the particle, and i represents any particle in the particle swarm; v_{id} is the velocity of the above particles at the corresponding position; p_{id} is the optimal position of the above particles under this condition, and p_{gd} is the global optimal position under the current condition.

(6) Return to Simulink model: return the optimized parameters a_6 and t_f to the trajectory in Simulink to obtain the trajectory with the lowest vibration.

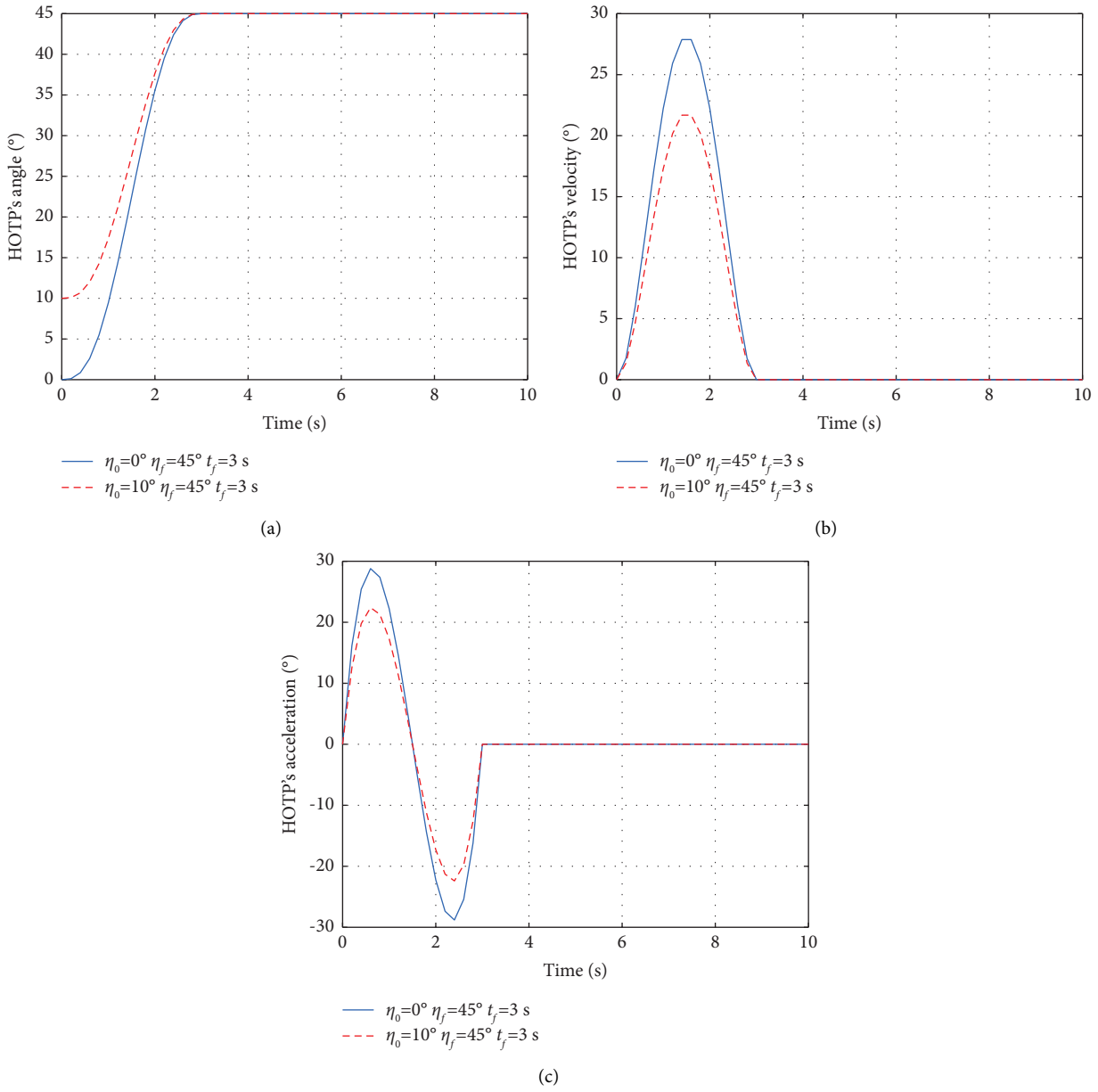

Figure 6: HOTP's trajectory for change initial angle based on Case 2. (a) HOTP's angle. (b) HOTP's velocity. (c) HOTP's acceleration.

(7) Run the vibration effect: substitute the optimal trajectory into the model of the robotic arm, and run it through Simulink to obtain the final vibration error diagram.

Define $0 < t_f < 5$. In order to ensure the monotonically increasing trajectory of the motor within the planned time, combined with equation (20), it can be deduced that $0 \le \varepsilon_6 \le 1$. Parameters from Table 2 are selected for comparison with the optimal values. The simulation results are shown in Figure 8. The optimal values of t_f and ε_6 are determined through the PSO algorithm. Figure 8(a) shows that the optimal parameters $t_f = 2.928$ and $\varepsilon_6 = 0.0039761$ can be obtained through 3 iterations of the PSO algorithm. Figure 8(b) can prove that the proposed HTOP can achieve the optimal vibration suppression effect at $t_f = 2.928$ and $\varepsilon_6 = 0.0039761$. The results in Figure 8(c) demonstrate that, based on the cubic spline trajectory, the vibration amplitude of the FJM reaches approximately 1.8 mm. In contrast, the proposed HOTP trajectory effectively suppresses the vibration to only 0.02 mm. This significant reduction in vibration amplitude highlights the outstanding performance of the HOTP trajectory in vibration attenuation during motor operation. Furthermore, the comparison with parameters from Table 2 further validates the effectiveness of the proposed approach in achieving optimal motor performance. In summary, the HOTP trajectory proposed in this paper not only ensures a monotonically increasing trajectory of the motor within the specified time but also minimizes vibration, thereby enhancing the overall stability and efficiency of the motor system.

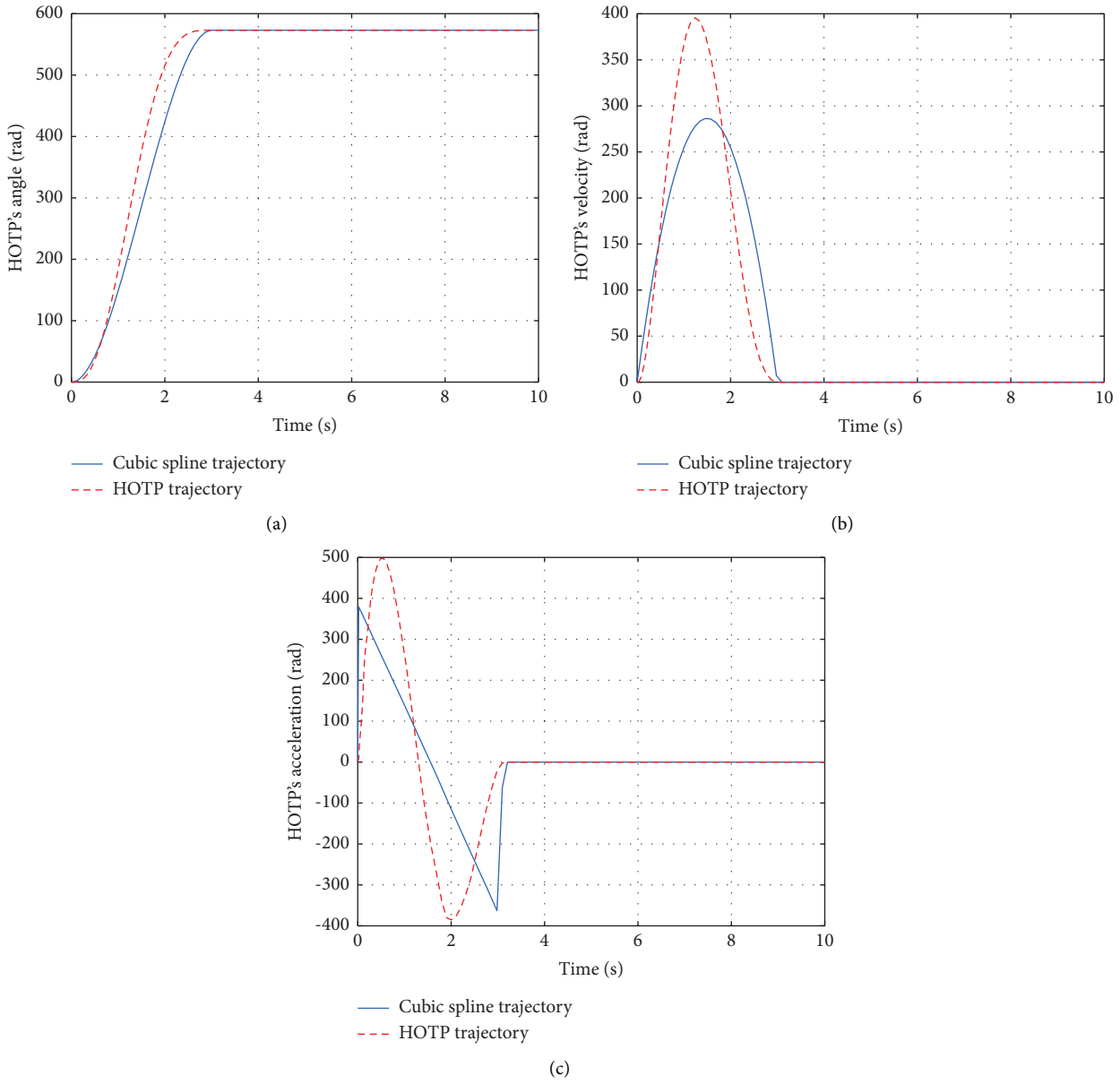

Figure 7: Comparison between HOTP trajectory and cubic spline trajectory based on Case 3. (a) Angle of HOTP trajectory and cubic spline trajectory. (b) Velocity of HOTP trajectory and cubic spline trajectory. (c) Acceleration of HOTP trajectory and cubic spline trajectory.

Table 2: t_f and ε_6 parameter values.

t_f (From small to large)	0.56	1.87	2.928	3.67
ε_6 (From large to small)	1	0.05	0.0039761	0.01

4.2. Simulation Results of Trajectory Tracking Control. To verify the advantages of the proposed fixed-time NTSMC, this section compares it with the finite-time NTSMC in [44]. After optimizing the PSO algorithm vibration in Section 2, we can obtain the optimal trajectory of the FJM's joint as follows:

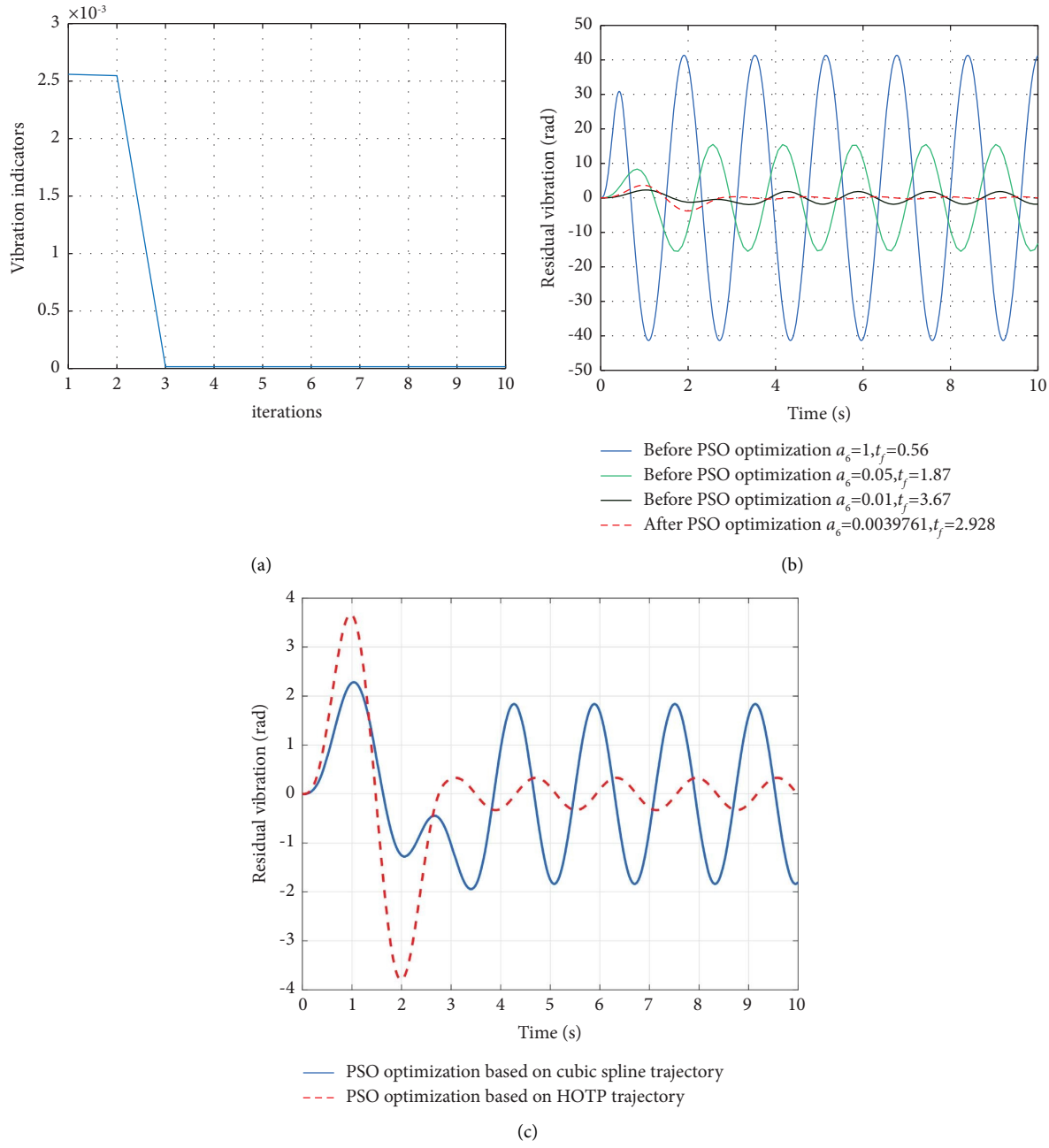

FIGURE 8: Optimization simulation of vibration suppression for FJM's Joint. (a) PSO algorithm optimization iterations. (b) Comparison of residual vibrations. (c) Comparison of residual vibrations between HOTP's trajectory and cubic spline trajectory.

$$\begin{cases} \widetilde{\vartheta} = (\eta_f - \eta_0)\sum_{i=0}^{6} \varepsilon_i \left(\frac{t}{t_f}\right)^i + \eta_0, \\ \varepsilon_0 = \varepsilon_1 = \varepsilon_2 = 0, \\ \varepsilon_3 = 10 - \varepsilon_6, \\ \varepsilon_4 = -15 + 3\varepsilon_6, \\ \varepsilon_5 = 6 - 3\varepsilon_6, \\ \varepsilon_6 = 4.2146 \times 10^{-3}. \end{cases} \tag{58}$$

As described in [44], the sliding surface and controller of the finite-time NTSMC scheme are

$$\begin{aligned} s &= e_2 + \int q_1 |e_1|^{\alpha_1} \operatorname{sgn}(e_1) + q_2 |e_2|^{\alpha_2} \operatorname{sgn}(e_2) dt, \\ u &= -\varphi - q_1 |e_1|^{\alpha_1} \operatorname{sgn}(e_1) - q_2 |e_2|^{\alpha_2} \operatorname{sgn}(e_2) - \kappa_1 \operatorname{sgn} s - \kappa_2 s, \end{aligned} \tag{59}$$

where $\operatorname{sgn}(s) = 2((1/(1+\exp^{-\omega s_i})) - (1/2))$, $\omega = 30$.

The controller parameters for finite-time NTSMC are set to

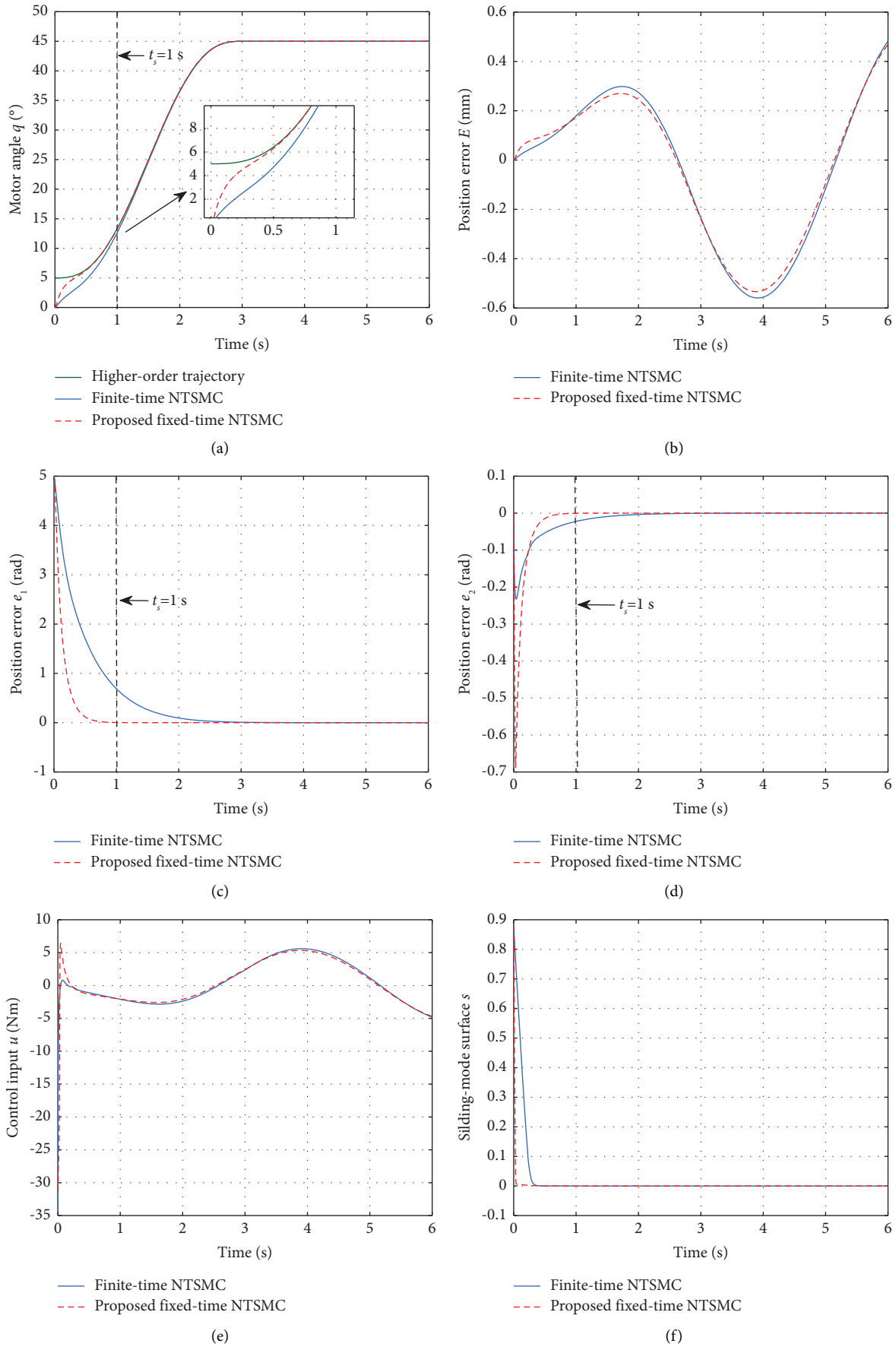

FIGURE 9: Track tracking control results with $\eta_0 = 5^\circ$, $\eta_f = 45^\circ$, $t_s = 1s$. (a) Motor angle q. (b) Residual vibration E. (c) Position error e_1. (d) Position error e_2. (e) Control input u. (f) Sliding-mode surface s.

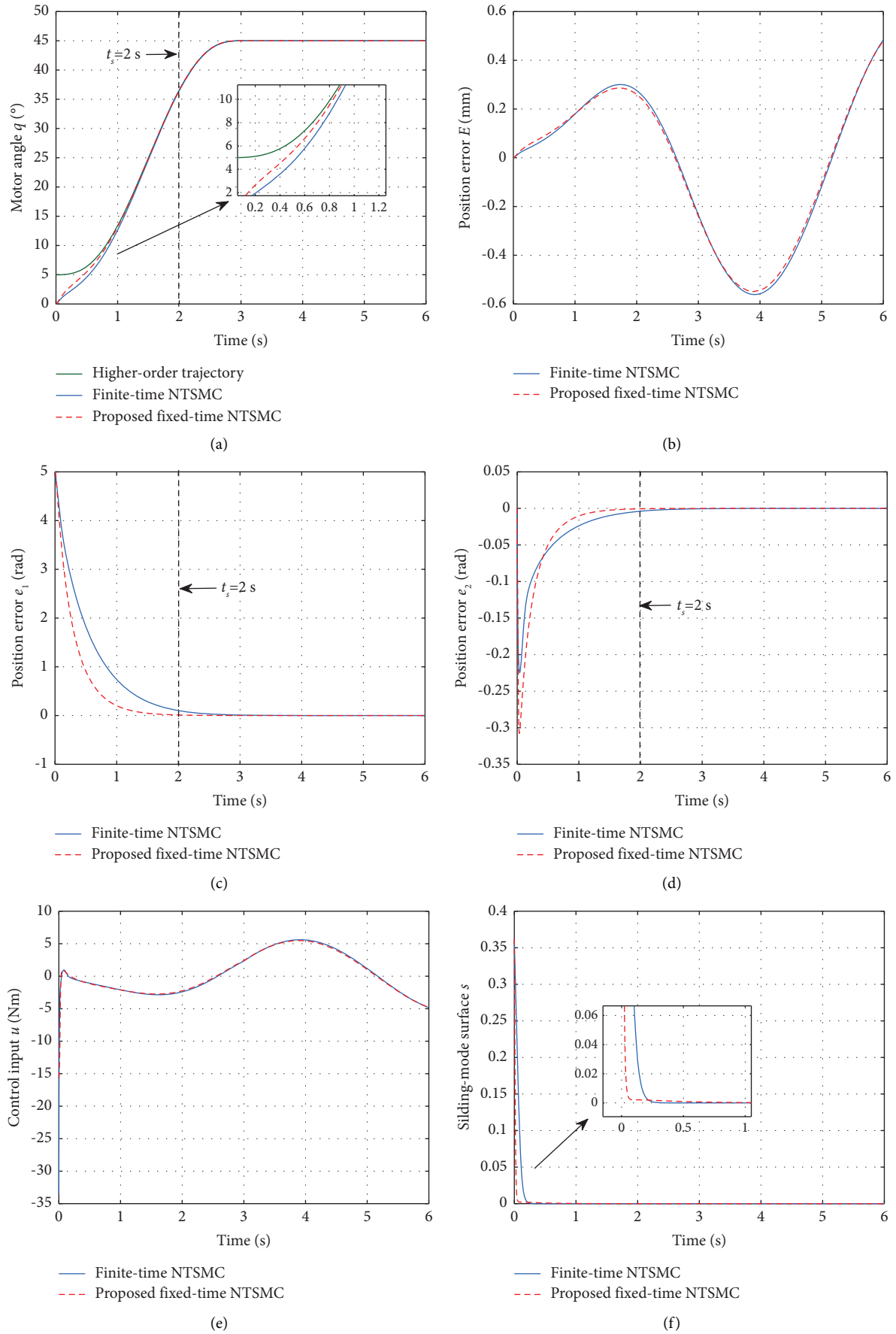

FIGURE 10: Track tracking control results with $\eta_0 = 5^\circ$, $\eta_f = 45^\circ$, $t_s = 2s$. (a) Motor angle q. (b) Residual vibration E. (c) Position error e_1. (d) Position error e_2. (e) Control input u. (f) Sliding-mode surface s.

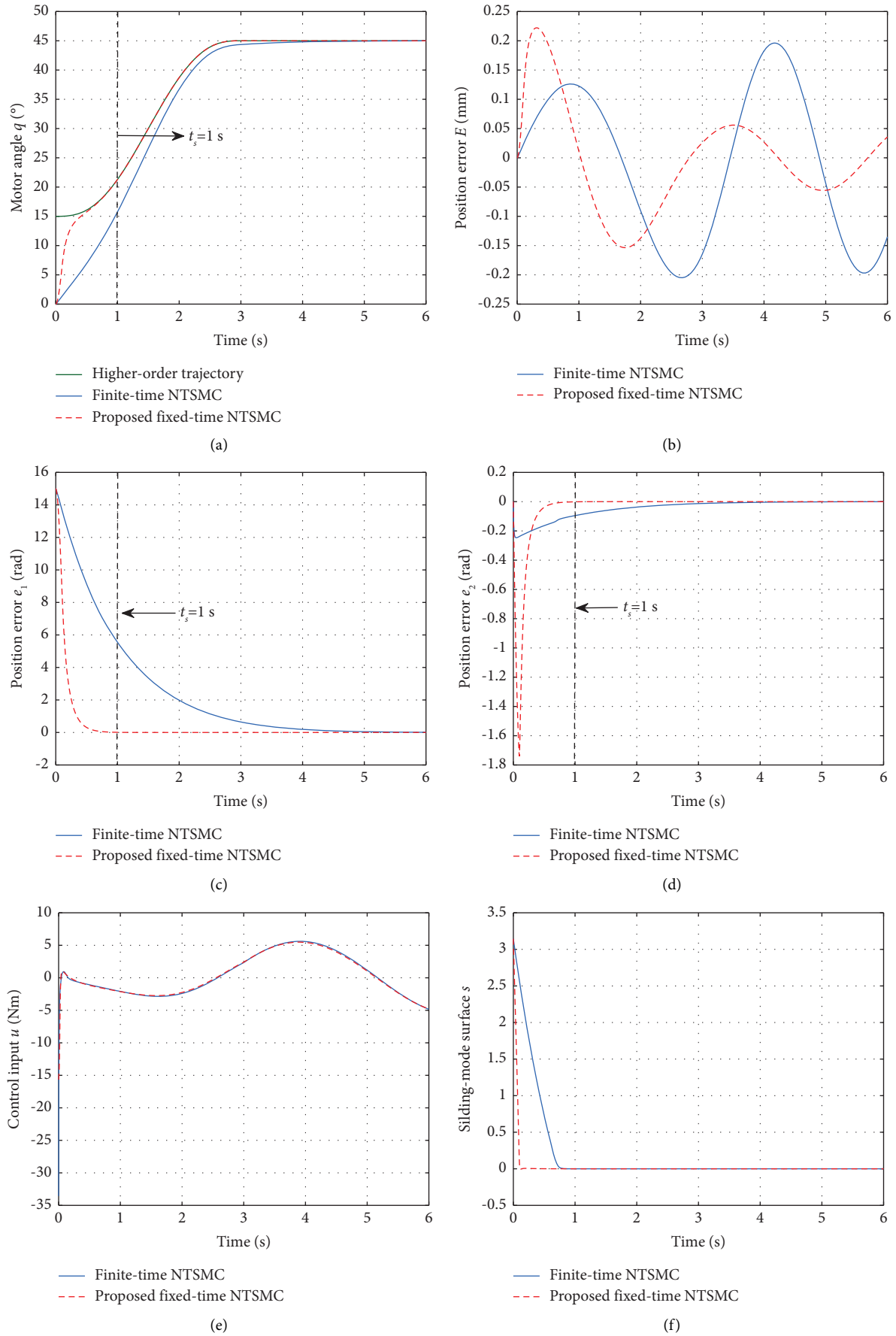

FIGURE 11: Track tracking control results with $\eta_0 = 15^\circ$, $\eta_f = 45^\circ$, $t_s = 1s$. (a) Motor angle q. (b) Residual vibration E. (c) Position error e_1. (d) Position error e_2. (e) Control input u. (f) Sliding-mode surface s.

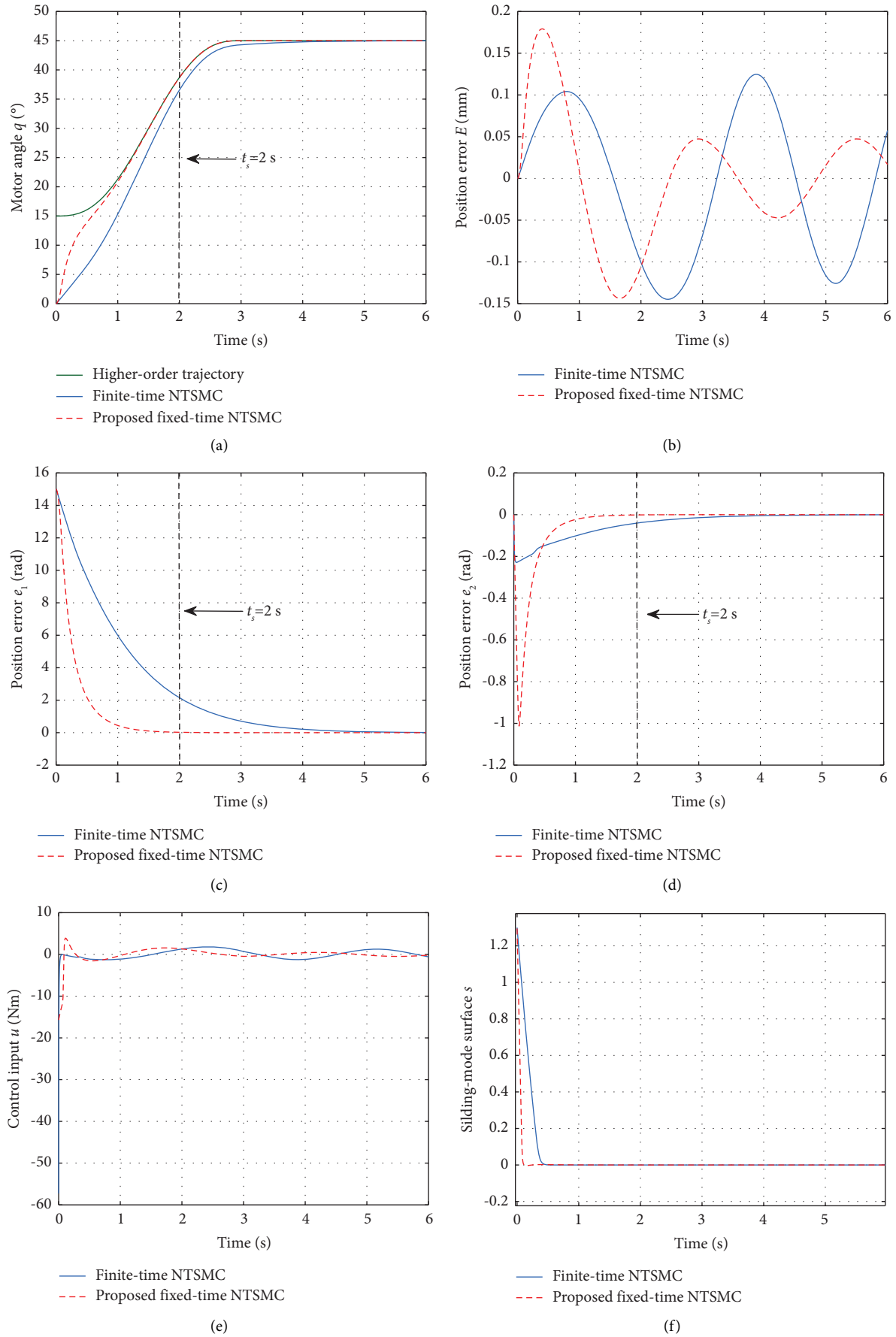

FIGURE 12: Track tracking control results with $\eta_0 = 15^\circ$, $\eta_f = 45^\circ$, $t_s = 2s$. (a) Motor angle q. (b) Residual vibration E. (c) Position error e_1. (d) Position error e_2. (e) Control input u. (f) Sliding-mode surface s.

$$\begin{cases} q_1 = 70, \\ q_2 = 90, \\ \alpha_1 = 0.2, \\ \alpha_2 = 0.3, \\ \kappa_1 = 3, \\ \kappa_2 = 1. \end{cases} \tag{60}$$

Case 1 (Small initial angle): In this case, consider the situation where the initial planning angle is small, the given initial angle is $\eta_0 = 5^\circ$, the target angle is $\eta_f = 45^\circ$. Meanwhile, consider the impact of T_s on trajectory tracking under different parameters and analyze the two cases of $T_s = 1$ and $T_s = 2$. The simulation results are shown in Figures 9 and 10. The fixed-time NTSMC parameters are set to $\alpha = 0.6$, $\xi = 0.55$, $T_e = 0.3$, and $\alpha_s = 0.1$. When $T_s = 1$, the joint trajectory of FJM will track the optimal trajectory before 1s, From Figure 9(a), it can be seen that fixed-time NTSMC can track the optimal trajectory at 0.5 s. From Figures 9(c) and 9(d), it can be seen that the trajectory error e_1 and e_2 converges to 0 within 1s. The sliding surface will be convergent to 0 within 0.3s. The residual vibration of FJM remains consistent with the optimal trajectory vibration, with a vibration amplitude of 0.5 mm.

When $T_s = 2$, the joint trajectory of FJM will track the optimal trajectory before 2s. From Figure 10(a), it can be seen that the fixed-time NTSMC can track the optimal trajectory at 1.2s, while the vibration of FJM can still maintain the word 0.5 mm. From Figures 10(c) and 10(d), it can be seen that the trajectory error e_1 and e_2 converges to 0 within 2s, and the sliding surface will converge to 0 at $T_e = 0.3$.

Case 2 (large initial angle): Compared to Case 1, increase the initial angle of the trajectory significantly to $\eta_0 = 15^\circ$, the target angle is $\eta_f = 45^\circ$. Analyze the two cases of $T_s = 1$ and $T_s = 2$. Figures 11 and 12 show the simulation results of Case 2. When $T_s = 1$ and $T_s = 2$, it can be seen from Figures 11 and 12 that the system trajectory can still converge to 0 within a fixed time, unaffected by changes in the initial value of the trajectory. However, the finite time is affected by the initial value of the system. When the initial trajectory changes from $\eta_0 = 5^\circ$ to $\eta_0 = 15^\circ$, the finite time can only converge to 0 within 4s. In addition, the vibration amplitude of FJM will decrease to 0.05 mm. Therefore, this scheme can meet the working requirements of FJM when the initial trajectory value is large.

5. Conclusion

Vibration suppression and trajectory tracking control of the FJM based on the PSO algorithm and fixed-time control are proposed in this paper. The feasibility of this method has been verified through numerical simulation, which indeed reduces the vibration between the joint trajectory and the motor trajectory and improves the precise control effect of FJM. However, because FJM is a strongly coupled system, the system parameters are too complex, and there are various interferences during the motion process, which makes it impossible to completely eliminate the vibration and can only be optimized as much as possible. Due to the complexity and high cost of the FJM experimental system, completion within a short timeframe is challenging. Anticipating improved laboratory conditions in the future, we plan to apply the proposed solution to multi-link robotic arm systems. These arms will find widespread application in production lines, handling complex assembly and processing of parts, as well as in intricate minimally invasive surgeries. We will persistently tackle complex issues in real systems, including unmodeled complexities, uncertainties, diverse working environments, and the high computational demands of real-time algorithms. By applying the solution to real-world scenarios, we aim to demonstrate the adaptability and robustness of the approach in future multi-link systems, laying a foundation for seamless integration of theory and practical implementation.

Appendix

A. Proof of Theorem 1

Proof

Step 1: A Lyapunov function can be defined as

$$v = \frac{1}{2}s^2. \tag{A.1}$$

According to equation (A.1), the time derivative of v can be calculated as

$$\begin{aligned} \dot{v} = s\dot{s} &= -s\left(\frac{\pi}{2T_s\alpha_s}\left(\mathrm{Sig}(s)^{1+\alpha_s} + \mathrm{Sig}(s)^{1-\alpha_s}\right)\right) \\ &= -\frac{\pi}{2T_s\alpha_s}\left(v^{((1+\alpha_s)/2)} + v^{((1-\alpha_s)/2)}\right) \end{aligned} \tag{A.2}$$

Therefore,

$$v = s = 0, \quad \text{if } t = \frac{2T_s}{\pi}\arctan\left(|x(0)|^\alpha\right), \tag{A.3}$$

$$v = s = 0, \quad t \le T_s. \tag{A.4}$$

Step 2: Combining (A.3) and (49), e_2 can be represented as

$$e_2 = -\frac{\pi}{2(T_e - T_s)_e\alpha}\left(f_{e1} + \mathrm{sig}(e_1)^{1+\alpha}\right). \tag{A.5}$$

For $|e_1| \ge \xi$, we have

$$e_2 = -\frac{\pi}{2(T_e - T_s)\alpha}\left(\mathrm{sig}(e_1)^{1-\alpha} + \mathrm{sig}(e_1)^{1+\alpha}\right), \quad \text{if } t \ge \varepsilon T_s, \tag{A.6}$$

where $\varepsilon = (2/\pi)\arctan(|x(0)|^\alpha)$.

For $|e_1| < \xi$, we have

$$|e_1| < \xi, \quad \text{if } t \geq \varepsilon T_s + \gamma(T_e - T_s), \tag{A.7}$$

where $\gamma = (2/\pi)\arctan(|x(T_s)|^{\alpha})$.

When $\varepsilon < \gamma$

$$|e_1| < \xi, \quad \text{if } t \geq \gamma T_s. \tag{A.8}$$

And, we have

$$s = 0, t \geq \gamma T_s. \tag{A.9}$$

Then, combining (50), (A.5), (A.8), and (A.9), we have

$$e_2 = -\frac{\pi}{2T_s\alpha}\left(\frac{-1-\ln\xi}{1-\alpha-\xi\ln\xi}\mathrm{Sig}(e_1)^{2-\alpha} + \frac{\xi^{-2\alpha+|e_1|}}{1-\alpha-\xi\ln\xi}e_1 + \mathrm{Sig}(e_1)^{1+\alpha}\right), \quad \text{if } t \geq \gamma T_s. \tag{A.10}$$

A new Lyapunov function is defined as

$$H = \frac{1}{2}e_1^2. \tag{A.11}$$

Then, the time derivative of equation (A.11) can be calculated by considering equation (A.10) as

$$\begin{aligned}\dot{H} = e_1 e_2 &= -\frac{\pi}{2T_s\alpha}\left(\frac{-1-\ln\xi}{1-\alpha-\xi\ln\xi}|e_1|^{3-\alpha} + \frac{\xi^{-2\alpha+|e_1|}}{1-\alpha-\xi\ln\xi}|e_1|^2 + |e_1|^{2+\alpha}\right)\\ &= -\frac{\pi}{2T_s\alpha}\left(\frac{-1-\ln\xi}{1-\alpha-\xi\ln\xi}|e_1|^{3-\alpha} - \frac{\pi}{2T_s\alpha}\frac{\xi^{-2\alpha+|e_1|}}{1-\alpha-\xi\ln\xi}|e_1|^2 + |e_1|^{2+\alpha}\right).\end{aligned} \tag{A.12}$$

As $\xi \in (0, 1/e)$, $\alpha \in (0,1)$, we have

$$\frac{-1-\ln\xi}{1-\alpha-\xi\ln\xi} > 0, \tag{A.13}$$

$$\frac{\xi^{-2\alpha+|e_1|}}{1-\alpha-\xi\ln\xi} > 0. \tag{A.14}$$

Considering (A.8) and $\xi \in (0, 1/e)$, we have

$$\xi^{|e_1|} < \xi^{\xi}, \quad \text{if } t \geq \gamma T_s. \tag{A.15}$$

Then, combining (A.12)–(A.15), we have

$$\dot{H} \leq -g_{e1}H, \quad \text{if } t \geq \gamma T_s, \tag{A.16}$$

where the constant $g_{e1} = (\xi^{-2\alpha}/2(1-\alpha-\xi\ln\xi))\xi > 0$.

From (A.16), we have

$$H \leq H(\gamma T_s)e^{-g_{e1}(t-\gamma T_s)}, \quad \text{if } t \geq \gamma T_s. \tag{A.17}$$

Thus, combining $|e_1| < \xi$, if $t \geq \gamma T_s$, we have $H(\infty) = 0$, the proof is finished. □

Data Availability

The data used to support the findings of this study are included within the article.

Conflicts of Interest

The authors declare that they have no conflicts of interest.

Acknowledgments

This work was supported by Young Talent Fund of Association for Science and Technology in Xi'an (Program No. 095920221378), the Scientific Research Fund for High-Level Talents of Xijing University (XJ22B01), the Scientific Research Program Funded by Education Department of Shaanxi Provincial Government (23JK0706), the Scientific Research Foundation of Xijing University (XJ230108), and the Horizontal Project (2024610002002867).

References

[1] H. Ullah, F. M. Malik, A. Raza et al., "Robust output feedback control of single-link flexible-joint robot manipulator with matched disturbances using high gain observer," *Sensors*, vol. 21, no. 9, p. 3252, 2021.

[2] K. Jayaswal, D. K. Palwalia, and S. Kumar, "Performance investigation of PID controller in trajectory control of two-link robotic manipulator in medical robots," *Journal of Interdisciplinary Mathematics*, vol. 24, no. 2, pp. 467–478, 2021.

[3] L. Liu, W. Yao, and Y. Guo, "Prescribed performance tracking control of a free-flying flexible-joint space robot with

disturbances under input saturation," *Journal of the Franklin Institute*, vol. 358, no. 9, pp. 4571–4601, 2021.

[4] X. F. Liu, X. Y. Zhang, G. P. Cai, and W. J. Chen, "Capturing a space target using a flexible space robot," *Applied Sciences*, vol. 12, no. 3, p. 984, 2022.

[5] M. Mazare, S. Tolu, and M. Taghizadeh, "Adaptive variable impedance control for a modular soft robot manipulator in configuration space," *Meccanica*, vol. 57, no. 1, pp. 1–15, 2022.

[6] M. Shi, Y. Cheng, B. Rong, W. Zhao, Z. Yao, and C. Yu, "Research on vibration suppression and trajectory tracking control strategy of a flexible link manipulator," *Applied Mathematical Modelling*, vol. 110, pp. 78–98, 2022.

[7] Y. Huang, W. Chen, and M. Shao, "Tracking and vibration control of a free-floating space manipulator system with flexible links and joints," *Proceedings of the Institution of Mechanical Engineers, Part G: Journal of Aerospace Engineering*, vol. 236, no. 7, pp. 1361–1374, 2022.

[8] L. Zhang, Y. Wang, X. Zhao, P. Zhao, and L. He, "Time-optimal trajectory planning of serial manipulator based on adaptive cuckoo search algorithm," *Journal of Mechanical Science and Technology*, vol. 35, no. 7, pp. 3171–3181, 2021.

[9] Y. Zhao, J. Mei, and W. Niu, "Vibration error-based trajectory planning of a 5-dof hybrid machine tool," *Robotics and Computer-Integrated Manufacturing*, vol. 69, Article ID 102095, 2021.

[10] A. Abe, "Trajectory planning for residual vibration suppression of a two-link rigid-flexible manipulator considering large deformation," *Mechanism and Machine Theory*, vol. 44, no. 9, pp. 1627–1639, 2009.

[11] T. Zhang, M. Zhang, and Y. Zou, "Time-optimal and smooth trajectory planning for robot manipulators," *International Journal of Control, Automation and Systems*, vol. 19, no. 1, pp. 521–531, 2021.

[12] T. Chettibi, "Smooth point-to-point trajectory planning for robot manipulators by using radial basis functions," *Robotica*, vol. 37, no. 3, pp. 539–559, 2019.

[13] N. Sun, Y. Fang, Y. Zhang, and B. Ma, "A novel kinematic coupling-based trajectory planning method for overhead cranes," *IEEE/ASME Transactions on Mechatronics*, vol. 17, no. 1, pp. 166–173, 2012.

[14] Q. Meng, X. Lai, Z. Yan, Y. Wang, and M. Wu, "Position control with zero residual vibration for two degrees-of-freedom flexible systems based on motion trajectory optimization," *Information Sciences*, vol. 575, pp. 698–713, 2021.

[15] L. Cui, H. Wang, and W. Chen, "Trajectory planning of a spatial flexible manipulator for vibration suppression," *Robotics and Autonomous Systems*, vol. 123, Article ID 103316, 2020.

[16] G. Wu, W. Zhao, and X. Zhang, "Optimum time-energy-jerk trajectory planning for serial robotic manipulators by reparameterized quintic NURBS curves," *Proceedings of the Institution of Mechanical Engineers-Part C: Journal of Mechanical Engineering Science*, vol. 235, no. 19, pp. 4382–4393, 2021.

[17] Q. Meng, X. Lai, Z. Yan, C. Y. Su, and M. Wu, "Motion planning and adaptive neural tracking control of an uncertain two-link rigid–flexible manipulator with vibration amplitude constraint," *IEEE Transactions on Neural Networks and Learning Systems*, vol. 33, no. 8, pp. 3814–3828, 2022.

[18] Q. Chang, H. Wang, D. Wang, H. Zhang, K. Li, and B. Yu, "Motion planning for vibration reduction of a railway bridge maintenance robot with a redundant manipulator," *Electronics*, vol. 10, no. 22, p. 2793, 2021.

[19] B. Nadir, O. Mohammed, N. Minh-Tuan, and S. Abderrezak, "Optimal trajectory generation method to find a smooth robot joint trajectory based on multiquadric radial basis functions," *The International Journal of Advanced Manufacturing Technology*, vol. 120, no. 1-2, pp. 297–312, 2022.

[20] T. Rybus, M. Wojtunik, and F. L. Basmadji, "Optimal collision-free path planning of a free-floating space robot using spline-based trajectories," *Acta Astronautica*, vol. 190, pp. 395–408, 2022.

[21] A. Shrivastava and V. K. Dalla, "Failure control and energy optimization of multi-axes space manipulator through genetic algorithm approach," *Journal of the Brazilian Society of Mechanical Sciences and Engineering*, vol. 43, no. 10, pp. 445–517, 2021.

[22] X. Yu, X. Ye, and S. Zhang, "Floating pollutant image target extraction algorithm based on immune extremum region," *Digital Signal Processing*, vol. 123, Article ID 103442, 2022.

[23] D. Shang, X. Li, M. Yin, and F. Li, "Control method of flexible manipulator servo system based on a combination of RBF neural network and pole placement strategy," *Mathematics*, vol. 9, no. 8, p. 896, 2021.

[24] J. Oliveira, P. M. Oliveira, J. Boaventura-Cunha, and T. Pinho, "Chaos-based grey wolf optimizer for higher order sliding mode position control of a robotic manipulator," *Nonlinear Dynamics*, vol. 90, no. 2, pp. 1353–1362, 2017.

[25] X. Meng and X. Zhu, "Autonomous obstacle avoidance path planning for grasping manipulator based on elite smoothing ant colony algorithm," *Symmetry*, vol. 14, no. 9, p. 1843, 2022.

[26] H. Sun, X. Tang, and J. Wei, "Vibration suppression for large-scale flexible structures using deep reinforcement learning based on cable-driven parallel robots," *ASME International Mechanical Engineering Congress and Exposition*, vol. 84546, pp. 16–19, Article ID V07AT07A035, 2020.

[27] M. M. İlman and Y. S. Arıkuşu, "COVID-19 optimization-based vibration controller for a flexible manipulator," *Trends, Paradigms, and Advances in Mechatronics Engineering*, vol. 93, no. 109, p. 17, 2023.

[28] M. M. İlman, Ş. Yavuz, and P. Y. Taser, "Generalized input preshaping vibration control approach for multi-link flexible manipulators using machine intelligence," *Mechatronics*, vol. 82, Article ID 102735, 2022.

[29] X. H. Liu, D. Zhang, J. Zhang, T. Zhang, and H. Zhu, "A path planning method based on the particle swarm optimization trained fuzzy neural network algorithm," *Cluster Computing*, vol. 24, no. 3, pp. 1901–1915, 2021.

[30] C. Duan, J. Feng, and H. Chang, "Meteorology-aware path planning for the UAV based on the improved intelligent water drops algorithm," *IEEE Access*, vol. 9, pp. 49844–49856, 2021.

[31] B. Sun, D. Zhu, C. Tian, and C. Luo, "Complete coverage autonomous underwater vehicles path planning based on glasius bio-inspired neural network algorithm for discrete and centralized programming," *IEEE Transactions on Cognitive and Developmental Systems*, vol. 11, no. 1, pp. 73–84, 2019.

[32] Ş. Yavuz, M. M. İlman, and B. Binici, "Modeling approach and analysis time comparison of single-link flexible steel- and epoxy-glass/carbon-fiber composite manipulators," *Structures*, vol. 26, pp. 396–405, 2020.

[33] N. Wongvanich, N. Roongmuanpha, and W. Tangsrirat, "Extended exploration grey wolf optimization, CFOA-based circuit implementation of the sigr function and its applications in finite-time terminal sliding mode control," *IEEE Access*, vol. 11, pp. 88388–88402, 2023.

[34] L. Zhang, R. Tao, Z. X. Zhang, Y. R. Chien, and J. Bai, "PMSM non-singular fast terminal sliding mode control with

disturbance compensation," *Information Sciences*, vol. 642, Article ID 119040, 2023.

[35] B. Alizadeh, A. Hajipour, H. Tavakoli, and A. Nasrabadi, "Robust trajectory tracking of Delta parallel robot using fractional-order sliding mode control," *IEEE Access*, vol. 11, pp. 86397–86412, 2023.

[36] F. Li, Z. Zhang, Y. Wu, Y. Chen, K. Liu, and J. Yao, "Improved fuzzy sliding mode control in flexible manipulator actuated by PMAs," *Robotica*, vol. 40, no. 8, pp. 2683–2696, 2022.

[37] Y. Xu, X. Wang, L. Wang, K. Wang, and L. Ma, "Learning control for flexible manipulators with varying loads: A composite method with robust adaptive dynamic programming and robust sliding mode control," *Electronics*, vol. 11, no. 6, p. 956, 2022.

[38] W. Alam, N. Ali, H. M. W. Aziz, and J. Iqbal, "Control of flexible joint robotic manipulator: design and prototyping," in *Proceedings of the International Conference on Electrical Engineering (ICEE)*, pp. 1–6, Dhaka, Bangladesh, February 2018.

[39] A. Mughees and I. Ahmad, "Multi-optimization of novel conditioned adaptive barrier function integral terminal SMC for trajectory tracking of a quadcopter System," *IEEE Access*, vol. 11, pp. 88359–88377, 2023.

[40] R. F. A. Khan, K. Rsetam, Z. Cao, and Z. Man, "Singular perturbation-based adaptive integral sliding mode control for flexible joint robots," *IEEE Transactions on Industrial Electronics*, vol. 70, no. 10, pp. 10516–10525, 2023.

[41] A. B. Alhassan, R. Chancharoen, B. B. Muhammad, and G. Phanomchoeng, "Precise automation of rotary flexible link manipulator using hybrid input shaping with single state feedback fuzzy logic and sliding mode controllers," *IEEE Access*, vol. 11, pp. 86711–86726, 2023.

[42] J. Liu, Y. Yang, X. Li, K. Zhao, Z. Yi, and Z. Xin, "Improved model-free continuous super-twisting non-singular fast terminal sliding mode control of IPMSM," *IEEE Access*, vol. 11, pp. 85361–85373, 2023.

[43] J. Tao, R. Liang, J. Su, Z. Xiao, H. Rao, and Y. Xu, "Dynamic event-triggered synchronization of Markov jump neural networks via sliding mode control," *IEEE Transactions on Cybernetics*, vol. 54, no. 4, pp. 2515–2524, 2024.

[44] H. Wang, H. Zhang, Z. Wang et al., "Sliding mode control of vertical double wall dividing-wall columns," *Chemical Engineering and Processing-Process Intensification*, vol. 182, Article ID 109200, 2022.

[45] H. Yang, J. W. Tang, and Y. R. Chien, "Application of new sliding mode control in vector control of PMSM," *IEICE Electronics Express*, vol. 19, no. 13, Article ID 20220156, 2022.

[46] W. Alam, S. Ahmad, A. Mehmood, and J. Iqbal, "Robust sliding mode control for flexible joint robotic manipulator via disturbance observer," *Interdisciplinary Description of Complex Systems*, vol. 17, no. 1, pp. 85–97, 2019.

[47] W. Alam, A. Mehmood, K. Ali, U. Javaid, S. Alharbi, and J. Iqbal, "Nonlinear control of a flexible joint robotic manipulator with experimental validation," *Strojniški vestnik-Journal of Mechanical Engineering*, vol. 64, no. 1, pp. 47–55, 2018.

[48] H. M. W. Aziz and J. Iqbal, "Flexible joint robotic manipulator: modeling and design of robust control law," in *Proceedings of the 2016 2nd International Conference on Robotics and Artificial Intelligence (ICRAI)*, pp. 63–68, IEEE, Islamabad, Pakistan, December 2016.

[49] O. Khan, M. Pervaiz, E. Ahmad, and J. Iqbal, "On the derivation of novel model and sophisticated control of flexible joint manipulator," *Revue Roumaine des Sciences Techniques-Serie Electrotechnique et Energetique*, vol. 62, no. 1, pp. 103–108, 2017.

[50] H. Hou, X. Yu, L. Xu, K. Rsetam, and Z. Cao, "Finite-time continuous terminal sliding mode control of servo motor systems," *IEEE Transactions on Industrial Electronics*, vol. 67, no. 7, pp. 5647–5656, 2020.

[51] M. I. Ullah, S. A. Ajwad, M. Irfan, and J. Iqbal, "Non-linear control law for articulated serial manipulators: simulation augmented with hardware implementation," *Elektronika ir Elektrotechnika*, vol. 22, no. 1, pp. 3–7, 2016.

[52] S. Ahmad, A. A. Uppal, M. R. Azam, and J. Iqbal, "Chattering free sliding mode control and state dependent Kalman filter design for underground gasification energy conversion process," *Electronics*, vol. 12, no. 4, p. 876, 2023.

[53] R. Afifa, S. Ali, M. Pervaiz, and J. Iqbal, "Adaptive backstepping integral sliding mode control of a mimo separately excited DC motor," *Robotics*, vol. 12, no. 4, p. 105, 2023.

[54] K. Rsetam, Z. Cao, and Z. Man, "Design of robust terminal sliding mode control for underactuated flexible joint robot," *IEEE Transactions on Systems, Man, and Cybernetics: Systems*, vol. 52, no. 7, pp. 4272–4285, 2022.

[55] K. Rsetam, Z. Cao, and Z. Man, "Cascaded-extended-state-observer-based sliding-mode control for underactuated flexible joint robot," *IEEE Transactions on Industrial Electronics*, vol. 67, no. 12, pp. 10822–10832, 2020.

[56] K. Rsetam, M. Al-Rawi, and Z. Cao, "Robust continuous sliding mode controller for uncertain canonical Brunovsky systems using reduced order extended state observer," in *Proceedings of the IEEE 20th International Conference on Industrial Informatics (INDIN)*, pp. 407–412, IEEE, Perth, Australia, July 2022.